IEEE Access
Multidisciplinary ⋮ Rapid Review ⋮ Open Access Journal

Received 31 August 2023, accepted 2 October 2023, date of publication 6 October 2023, date of current version 18 October 2023.

Digital Object Identifier 10.1109/ACCESS.2023.3322445

RESEARCH ARTICLE

Optimizing Massive MIMO Design for Non Uniform Traffic in Broadband Telecommunication Satellites Networks

PIERO ANGELETTI, (Senior Member, IEEE), AND RICCARDO DE GAUDENZI, (Fellow, IEEE)
European Space Agency, 2200 AG Noordwijk, The Netherlands

Corresponding author: Riccardo de Gaudenzi (rdegaude@gmail.com)

ABSTRACT There is a growing interest for satellites complementing the terrestrial networks for broadband access service provision. One of the key challenges is represented by the need to match the non uniform on-ground traffic distribution. This calls for exploiting large frequency reuse among the satellite beams and the adoption of interference mitigation through the use of precoding and/or efficient radio resource management techniques. In recent years, space technological developments have been making possible the implementation of active antennas operating at 20-30 GHz with a good level of efficiency thus opening up new perspectives in the flexible system and payload design. The presence of a large number of antenna radiating elements on-board the satellite stimulates the application of Massive Multiple Input Multiple Output (M-MIMO) techniques to satellite networks. In this paper, we extend previous work related to (pragmatic) M-MIMO adaptations for satellite broadband access networks and associated affordable complexity Radio Resource Management (RRM) algorithms. In particular, we cover the case of frequency colouring scheme and the optimization of the precoding in presence of non uniform traffic. We also enhance the system model to achieve more realistic and comprehensive analysis of the performance results by means of the generation of a generic spatial traffic distribution, a more accurate satellite antenna modelling for the RRM algorithm and emulating the channel estimation errors. A spatial derivation of the traffic request system satisfaction factor has been developed to enhance the analysis of the simulation results. All these enhancements are applied to the previously published non uniform synthetically generated traffic cases and to a more realistic study case corresponding to a Geostationary Equatorial Orbit (GEO) satellite covering Americas for which a novel system optimization methodology has been developed.

INDEX TERMS Antenna arrays, Massive Multiple Input Multiple Output (M-MIMO), radio access networks, resource management, satellite communication, telecommunications.

I. INTRODUCTION

There is a growing interest in exploiting satellite networks to complement the terrestrial telecom infrastructure over low densely populated areas including oceans. One of the key challenges is how to achieve an acceptable throughput/user at an affordable cost. This calls for increasing the satellite frequency reuse adopting multi-beam payloads of growing size, flexibility and complexity. Unfortunately, initially a lot of research related to High Throughput Satellite Networks (HTS) has been focusing on the exploitation of precoding techniques to maximize the frequency reuse capability combined with simple resource assignment techniques typically assuming uniform traffic distribution [1], [2], [3], [4], [5], [6]. Even with such simplified assumptions, practical implementation aspects of precoding such as channel matrix inversion and channel state information (CSI) estimation complexity, payload calibration errors, need for sharing users on the same physical layer frame, presence of multiple gateways for serving a single satellite are limiting its achievable performance.

Precoding requires an accurate CSI estimation, thus regular reporting from the user equipment and tight control of the

The associate editor coordinating the review of this manuscript and approving it for publication was Sandra Costanzo.

satellite payload radio frequency chains differential phase and amplitude error, to avoid performance degradation [3]. The CSI update rate is even higher for Low Earth Orbiting (LEO) satellites due to the system high orbital dynamic. The typical HTS downlink carrier high bit rate requires to multiplex several users' packets on the same physical layer frame. This means that the precoding coefficient will be applied to users' located in different beam geographical locations. This results in a precoding performance degradation compared to a single user precoding approach [4]. The feeder link of high throughput broadband satellite networks requires multiple geographically separated gateways to handle the aggregated beams throughput. Each gateway will serve a subset of the satellite beams, hence the precoding performance will be affected[1] [5]. The issue of limited number of beams precoded by each gateway can be alleviated by combining precoding and beam hopping [6].

The system capability to cope with realistic non uniform traffic distribution and its quantitative performance assessment is pivotal to ensure the efficient use of the scarce space segment power and bandwidth resources. Therefore, it is of paramount importance that the space segment flexibility and efficiency is achieved with an affordable system complexity increase. This represents a major research challenge.

In the recent past this issue has been dealt with by adapting the payload single feed per beam and power allocation [7], [8], [9], [10], [11]. The growing availability of phased-array active antenna (PAAA) technologies for the space segment of satellite broadband telecommunication networks is opening up new opportunities for its design methodology optimization. In particular, PAAA allows to drastically increase the space segment flexibility, hence its capability to cope with the spatially and time variant non uniform traffic to be served on ground. The presence of a large number of PAAA's radiating elements has been triggering the interest to investigate the potential advantages of exploiting Massive Multiple Input Multiple Output (M-MIMO) techniques to this kind of space systems. The above discussed issues affecting the practical precoding implementation in HTS networks has triggered the investigation of a pragmatic approaches for its implementation [12], [13], [14], [15].

Clearly the satellite mm-wave link is basically a white Gaussian channel, hence wiping out the potential M-MIMO channel hardening gain [16]. In [12] the authors have shown that, for a practical multibeam broadband satellite network, the bulk of Minimum Mean Square Error (MMSE) precoding M-MIMO gain can be achieved with a simpler payload architecture using Fast-Fourier Transform (FFT) type of fixed beamforming,[2] thus avoiding the MMSE associated computational complexity. This approach has been dubbed Pragmatic M-MIMO and largely deviates from the satellite M-MIMO precoding literature approach which is looking for ways to mitigate the precoding complexity implementation but not how to avoid it. In particular, M-MIMO CSI estimation complexity reduction adopting statistical CSI is investigated in [13]. The use of an hybrid analog/digital precoding exploiting the statistical CSI at the transmitter is investigated in [14]. Similarly to [12], the idea to use a codebook of FFT-based pre-computed beams for LEO satellites to ease the payload implementation has also been reported in [15]. However, the paper while recognizing that this approach has clear payload implementation advantages is leaving as further research the way to counteract the high level of co-channel interference.

A key driver for improving the PAAA performance for both, classical and Pragmatic M-MIMO in the presence of non-uniform traffic distribution, is the adoption of a high performance, yet affordable complexity, Radio Resource Management (RRM). The RRM plays a key role in distributing traffic in the system frequency, time and code dimensions to maximize the throughput reducing the system self-generated interference. As mentioned before, this issue attracted a number of contributions in the recent years. Reference [7] represents a first attempt to find a solution for the allocation of power and bandwidth in a single feed per beam multibeam HTS in the presence of uneven traffic request per beam. In this paper the non-convex optimization problem is tackled by means of an annealing algorithm. In [8] the above multibeam satellite power and bandwidth allocation issue is tackled adding to the unmet capacity the minimization of the total transmitted power transforming it in a nonconvex differentiable problem. The aspect of efficiently combing precoding and beam hopping for a single feed per beam HTS is tackled in [9]. To simplify the resource allocation optimization process, pre-defined cluster instead of single beams are hopped. To further reduce the combinatorial problem complexity, a graph theory approach is adopted. A more general approach in combining precoding with cluster hopping illumination pattern optimization for a beam-hopped HTS has been proposed in [10]. Three methods target the cross-beam interference minimization, such that the number of beams that need to be precoded are kept to minimal to mitigate system complexity. Reference [11] investigates the resource optimization problem in multibeam satellites. The non-deterministic polynomial-time (NP) hardness and inapproximability of the problem are demonstrated motivating the use of a two-stage metaheuristic approach.

The above references are dealing with the more classical single feed per beam HTS payloads not exploiting M-MIMO techniques thus providing less flexibility than the PAAA. Furthermore, despite the attempts for simplifiying the NP-hard RRM optimization problem, the proposed solutions are typically relying on sub-optimum iterative approaches. A first key contribution to further simplify the RRM problem for M-MIMO PAAA is reported in [17] and [18] where a quasi-optimum heuristic linear complexity RRM technique

[1]Typically the precoding is implemented at the gateway to reduce the on-board complexity burden.

[2]The presence of a fixed grid of beams covering the requested satellite coverage area avoids the need for a cumbersome MIMO channel (amplitude/phase) estimation. The only information required is a rough (few km accuracy) knowledge of the user equipment geographical location.

has been devised for the case of a beam hopped time division multiplexing, and shown to efficiently cope with synthetically generated non uniform traffic distributions. The simulation results reported in [17] indicate that the overall throughput achieved combining Pragmatic M-MIMO solution and Heuristic RRM (H-RRM), are only slightly below the ones achieved adopting the much more complex MMSE precoded M-MIMO even when both adopt the same optimized H-RRM solution. Considering the impact of the above mentioned practical MMSE implementation performance shortcomings and its much higher extra complexity, we have further arguments to further explore this pragmatic research path.

This paper extends previous work related to the pragmatic implementation of M-MIMO to multi-beam high throughput satellite broadband networks to further optimize its performance in the presence of arbitrary, yet more realistic non uniformly distributed traffic. In particular, we provide the following contributions:

- Extension of the H-RRM algorithm [17] to the case of a non beam hopped system. This is important as several modern HTS satellites exploiting on-board digital processors are adopting a more conventional frequency colouring scheme based on frequency instead of time division multiplexing required by a beam hopped system.
- Optimization of the Lagrange multiplier calculation for the MMSE type of precoding compared to the approach followed in [12] to make this upper performance theoretical bound even more stringent in the presence of non uniform traffic distribution.
- System model enhancement by: a) developing a more general traffic model that can follow any arbitrary (user defined) traffic distribution; b) deriving a more accurate multi-beam antenna model for further enhancing the H-RRM capabilty to cope with uneven traffic distribution; c) introducing a channel estimation error model for the MMSE precoding case to derive its sensitivity to channel estimation errors.
- Investigation on how to obtain a more realistic analysis of the throughput performance. This is achieved not just looking at the overall system throughput as in [17], but also at the derivation of the useful traffic spatial distribution. This allows the introduction as key performance indicator of the traffic request satisfaction factor representing the ratio between the offered and the requested throughput over the satellite coverage region.
- Analysis of a study case corresponding to a Geostationary Equatorial Orbit satellite (GEO) covering the Americas with realistic traffic spatial distribution to assess the validity of the above figures of merit. Given a target useful throughput, we derive a novel methodology for optimizing the system operating point taking advantage of the previously described improvements.

Although the numerical results reported in this paper are related to GEO satellites, the techniques illustrated can be easily adapted to systems adopting other type of orbits such as Low and Medium Earth Orbit ones. As mentioned before, the precoding implementation for such orbits is more challenging hence our proposed approach has an even higher potential for these cases.

The paper is organized as follows: Sec. II deals with the H-RRM extension to the FDM case and the Lagrange multiplier optimization for the MMSE type of precoding. Sec. III covers several system model enhancements such as the methodology for the generation of an arbitrary traffic distribution, a more accurate multi-beam antenna model for the H-RRM, and a channel estimation error model for the MMSE precoding case. The derivation of the useful traffic spatial distribution as well the traffic request satisfaction factor are also illustrated. Sec. IV provides numerical simulation results related to a realistic system study case exploiting the different aspects previously analytically derived.

II. EXTENSION OF THE M-MIMO AND H-RRM RESULTS

The objective of this section is to extend previous results related to pragmatic M-MIMO [12] and associated Heuristic Radio Resource Management (H-RRM) schemes [17] in the following areas:

- Pragmatic M-MIMO and Heuristic RRM extension to the Frequency Division Multiplexing (FDM) case;
- MMSE precoding Lagrange multiplier optimization.

A. PRAGMATIC M-MIMO AND HEURISTIC RRM EXTENSION TO THE FDM CASE

Although the pragmatic M-MIMO concept, initially devised for a Time Division Multiplexing (TDM) beam hopping (BH) system and the H-RRM [17], were claimed to be applicable to any multiplexing scheme, no specific implementation details were provided in the public literature. In the following we detail the way to implement (pragmatic) M-MIMO with H-RRM to the case of a multi-beam satellite system exploiting an FDM colouring scheme. The main difference between the two approaches lies in the nature of colours to which the H-RRM algorithm is applied. In BH-TDM the colour quantum managed by the RRM is represented by the time domain frame composing the TDM downlink carrier superframe. The number of colours C corresponds to the number of frames/superframe. Each active TDM frame carrier is occupying the full downlink bandwidth B_w^{TOT}, i.e. $B_w^{TDM} = B_w^{TOT}$ thus full frequency reuse among the active beams is implemented. The number of simultaneously active beams is represented by N_b^{tot}/C where N_b^{tot} represents the total number of served beams. Therefore, the available payload RF power P_T^c is used over the full downlink bandwidth B_w^{TOT}, i.e. $P_{TDM}^c = P_T^c$

Instead, in the FDM case, the colours are represented by the frequency sub-bands B_w^{FDM} in which the total downlink bandwidth B_w^{TOT} is segmented, i.e. $B_w^{FDM} = B_w^{TOT}/C$. Differently from the BH-TDM case, the carriers are continuously transmitted over the N_b^{tot} beams with a beam frequency reuse scheme (i.e. selection of active co-frequency beams)

managed by the H-RRM. In this case the available payload RF power P_T^c is equally partitioned in the C sub-bands, i.e. $P_{FDM}^c = P_T^c/C$.

The detailed RRM and beamforming/precoding analytical formulation extension to FDM for the forward link of a multiuser M-MIMO satellite network is reported in Appendix V-A. As shown in this Appendix, assuming the frequency response of the payload is flat in frequency, the H-RRM algorithm described in [17] can be simply applied independently to each sub-band. In the same Appendix it is shown that a sub-band customization of the H-RRM algorithm is required when the transponder frequency response is colour dependent.

It should be remarked that both BH-TDM and FDM schemes are also typically using a carrier time "slicing" to allow supporting different physical layer configurations (MODCODs in the DVB-S2 jargon [19]). This is because each active carrier is serving in TDM fashion the users located in the beam area experiencing different signal-to-noise plus interference ratio (SNIR). Hence Adaptive Coding and Modulation (ACM) allows to maximize the system throughput. However, for notation simplicity, this level of physical layer detail will be neglected in the following.

In the context of system design, the main difference between FDM and BH-TDM is the allocation of the available downlink bandwidth per user. In FDM, C is equal to the number of frequency sub-bands, and therefore the bandwidth per user/carrier is reduced by a factor C. On the other hand, in BH-TDM, the full beam bandwidth is available to a single user but only for a fraction $1/C$ of the time. So while the TDM concept of RRM resource slicing is also applicable to the FDM case, in the latter case the RRM has to decide which of the C sub-bands are activated in each available beam instead of which active beams with full bandwidth are active in a given TDM frame.

We recall here below the TDM throughput calculation approach followed in [12]

$$\overline{T}_{TDM} = \frac{1}{CN_{iter}} \sum_{n=1}^{N_{iter}} \sum_{c=1}^{C} \sum_{i=1}^{N_U(c)} T_{TDM}(c,i,n), \qquad (1)$$

where N_{iter} is the number of Monte Carlo simulations, C is the number of colours (frames in TDM), $N_U(c)$ is the number of active (TDM) carriers in the colour c and $T_{TDM}(c,i,n)$ is the simulated throughput for carrier n with colour c at simulation number i. The i-th user Shannon throughput is simply computed as

$$T_{TDM}^{SHA}(c,i,n) = R_s \log_2\left[1 + SNIR_{TDM}(c,i,n)\right], \qquad (2)$$

where R_s is the carrier baud rate,[3] $SNIR_{TDM}(c,i,n)$ represents the signal-to-interference plus noise ratio (SNIR) experienced by user i assigned to color c at iteration n. Instead, assuming the use of the DVB-S2X standard [19], the i-th user throughput is derived as

$$T_{TDM}^{S2X}(c,i,n) = R_s\ \eta_{S2X}\left[SNIR_{TDM}(c,i,n)\right], \qquad (3)$$

where the function η_{S2X} mapping the DVB-S2X standard [19] spectral efficiency as a function of the individual user SNIR. The details about the η_{S2X} function can be found in Appendix V-A of [12].

The FDM multi-beam satellite network throughput calculation requires some adaptation of (1) to account for the fact that the per colour throughput shall be summed and not averaged over the number of colours. This is different compared to TDM whereby the colours (time slices) are averaged out in (1) as they belong to different time frames of the superframe. It follows that

$$\overline{T}_{FDM} = \frac{1}{N_{iter}} \sum_{n=1}^{N_{iter}} \sum_{c=1}^{C} \sum_{i=1}^{N_U(c)} T_{FDM}(c,i,n), \qquad (4)$$

where $T_{FDM}(c,i,n)$ can be derived in a way similar to $T_{TDM}(c,i,n)$ for both Shannon and DVB-S2X cases.

Simulation findings are discussed in Sec. IV-A.

B. MMSE PRECODING LAGRANGE MULTIPLIER OPTIMIZATION

One point which has not been fully addressed in [12] is the way to optimize the Lagrange multiplier value λ appearing in the classical precoding MMSE equation

$$\mathbf{U}_{MMSE} = \left(\mathbf{H}^H\mathbf{H} + \lambda\mathbf{I}\right)^{-1}\mathbf{H}^H. \qquad (5)$$

The derivation of (5) and the choice of the optimal λ parameter depends on the formulation of the optimization problem for an arbitrary multiplexing scheme and/or traffic distribution. In non-statistical terms, the solution (5) can be considered a regularized version of the left pseudo-inverse where the $\lambda\mathbf{I}$ term is added as a perturbation to the Gram matrix $\mathbf{H}^H\mathbf{H}$ to render it invertible. Optimization of λ according to a SNIR criteria is described in [20]. A derivation of (5) as a power constrained MMSE transmit filter is reported in [21] where λ is the Lagrange multiplier associated to the power constraint. The close relationship to the MMSE detector is demonstrated in the uplink-downlink duality framework developed for characterizing the sum capacity of the Gaussian broadcast channel [22]. Following this last reference, under the hypothesis of identical power per user P_U, the optimal Lagrange multiplier corresponds to $\lambda = 1/P_U$ [2], [22].

In previous work the value $\lambda = 1$ has been adopted. While this value is quasi-optimal for the cases analyzed in [12] and when the traffic, although not uniform, is covering a large part of the multi-beam antenna coverage, this approximation becomes sub-optimum when the traffic region is a subset of the antenna coverage. This corresponds to the traffic cases 2-c/d/e/f configurations described in [17].

In practice, as mentioned in [17], the RRM algorithm serves a number N_U of users which is depending on the colour index c, i.e. $N_U(c)$. Hence the optimum value of λ is also

[3]The carrier baud rate is linked to the carrier bandwidth by the simple relation $R_s = B_w/(1+\rho)$, with $0 < \rho \leq 1$ being the transmitter square-root raised-cosine filter roll-off.

dependent on the colour index c. For this reason (6) can be generalized as a per colour equation

$$\mathbf{U}_{MMSE}(c) = \left[\mathbf{H}(c)^H\mathbf{H}(c) + \lambda(c)\mathbf{I}\right]^{-1}\mathbf{H}(c)^H, \quad \text{for } c = 1, \cdots C, \tag{6}$$

where $\lambda(c)$ optimal value corresponds to

$$\lambda(c) = \begin{cases} \dfrac{N_U(c)}{P^c_{TDM}} = \dfrac{N_U(c)}{P^c_T} & \text{for TDM} \\ \dfrac{N_U(c)}{P^c_{FDM}} = \dfrac{CN_U(c)}{P^c_T} & \text{for FDM.} \end{cases} \tag{7}$$

In Sec. IV-B we have been repeating the most relevant simulation results from [17] with this optimized Lagrange value to assess the associated performance improvement.

III. EXTENSION OF THE M-MIMO SYSTEM MODEL

In this section we extended the previously developed system model [12], [17] to encompass the following important aspects:

- A generic yet more realistic traffic distribution;
- An enhanced antenna model for the H-RRM algorithm;
- The imperfect channel estimation for precoding;
- The traffic request satisfaction analysis.

A. TRAFFIC MODEL GENERALIZATION

For a more realistic system model, it is necessary to generate an arbitrary user-defined random traffic distribution. To achieve this objective, we start from an input (experimental or business analysis-based) bi-dimensional discrete traffic distribution (not normalized), $\mathbf{T}_{tab}$, which is be provided in a tabular form (N_y rows and N_x columns) corresponding to a longitude-latitude grid with pixels of $\Delta lon \times \Delta lat$ area in square degrees. The tabular input $\mathbf{T}_{tab}$ is rearranged in the traffic matrix $\mathbf{T}_{x,y}$ with ordered Earth lat-lon coordinates x, y. The matrix $\mathbf{T}_{x,y}$ has dimension N_x and N_y. The rearranging process is pictorially shown in Fig. 1. To derive the traffic discrete two-dimensional probability distribution function (PDF) we normalize the matrix $\mathbf{T}_{x,y}$ of size $[N_x \times N_y]$ as

$$\mathbf{T}^{nor}_{x,y} = \frac{1}{\sum_{n_x=1}^{N_x}\sum_{n_y=1}^{N_y} t(n_x, n_y)}\mathbf{T}_{x,y}, \tag{8}$$

where $t(n_x, n_y)$ represents the generic row n_x and column n_y element of the matrix $\mathbf{T}_{x,y}$. We then convert the matrix $\mathbf{T}^{nor}_{x,y}$ in a on-dimensional PDF $\mathbf{p}_{t_{x,y}}$ with size $N_{xy} = N_x \cdot N_y$ by using the vec operator as

$$\mathbf{p}_{t_{x,y}} = vec\left[\mathbf{T}^{nor}_{x,y}\right] = \left[p_{t_{x,y}}(1), \cdots, p_{t_{x,y}}(N_{xy})\right]^T. \tag{9}$$

The corresponding discrete Cumulative Probability Distribution (CDF) can be computed as

$$P_{t_{x,y}}(n) = \sum_{m=1}^{n} p_{t_{x,y}}(m), \quad \text{with } 1 \le n \le N_{xy}. \tag{10}$$

Let ξ_i with $1 \le i \le N_U$ a random variable uniformly generated in $[0, 1]$, $\xi_i = \mathcal{U}(0, 1)$. We can now use the inversion sampling [23] of the uniform samples with respect to the one-dimensional traffic histogram $P_{t_{x,y}}$ to generate an integer-valued random variable $t_{rv}(i)$ of one-dimensional indexes as

$$t_{rv}(i) = P^{-1}_{t_{x,y}}(\xi_i), \tag{11}$$

with $t_{rv}(i) \in \mathbb{N}$, $1 \le t_{rv}(i) \le N_{xy}$.

At this point we can convert back the one-dimensional indexes $t_{rv}(i)$ to the bi-dimensional indexes $\left(n_x(i), n_y(i)\right) = \left(n_x(t_{rv}(i)), n_y(t_{rv}(i))\right)$ to obtain the random user grid coordinates in accordance to the traffic histogram. The random user position can be finally derived mapping the bi-dimensional indexes to the lon-lat coordinates and adding a dithering component for both x and y named $\epsilon_x(i)$, $\epsilon_y(i)$, corresponding to a bi-dimensional uniform distribution within the grid cell. It follows

$$\begin{aligned} lon_i &= lon_{min} + \Delta lon\left(n_x(i) - 1 + \epsilon_x(i)\right)\epsilon_x(i) = \mathcal{U}(0, 1) \\ lat_i &= lat_{min} + \Delta lat\left(n_y(i) - 1 + \epsilon_y(i)\right)\epsilon_y(i) = \mathcal{U}(0, 1), \end{aligned} \tag{12}$$

where

$$\begin{aligned} \Delta lon &= \frac{lon_{max} - lon_{min}}{N_x} \\ \Delta lat &= \frac{lat_{max} - lat_{min}}{N_y}. \end{aligned} \tag{13}$$

Once the user distribution is generated in lon-lat coordinates, standard coordinate transformations [24] can be used to convert (lon_i, lat_i) in satellite-centered spherical coordinates (ϑ_i, ϕ_i), and finally in antenna (u_i, v_i) coordinates (refer to Fig. 2) as

$$\begin{aligned} u_i &= \sin(\vartheta_i)\cos(\phi_i) \\ v_i &= \sin(\vartheta_i)\sin(\phi_i). \end{aligned} \tag{14}$$

Practical results for the above described generalized traffic model are presented in Sec. IV-C.

B. IMPROVEMENT OF THE ACTIVE ANTENNA PATTERN MODEL FOR THE H-RRM ALGORITHM

In [12] a simple Gaussian-based beam antenna pattern approximation has been used for the interference and SNIR computation required by the H-RRM algorithm. This is certainly an excellent approximation for the signal power calculation as it comes from the beam main lobe. Instead, for the interference calculation this pattern approximation is only accurate for the nearest interferers. In fact, although, for each location on the coverage area the main interference contribution is coming from adjacent beams main lobes, in general, the cumulative interference power from all active beams sidelobes should not be neglected. This is particularly true when the number of active beams is large as it is the case in high throughput systems. For this reason, in the following, a more accurate antenna model for periodic arrays enhancing the H-RRM algorithm performance is developed.

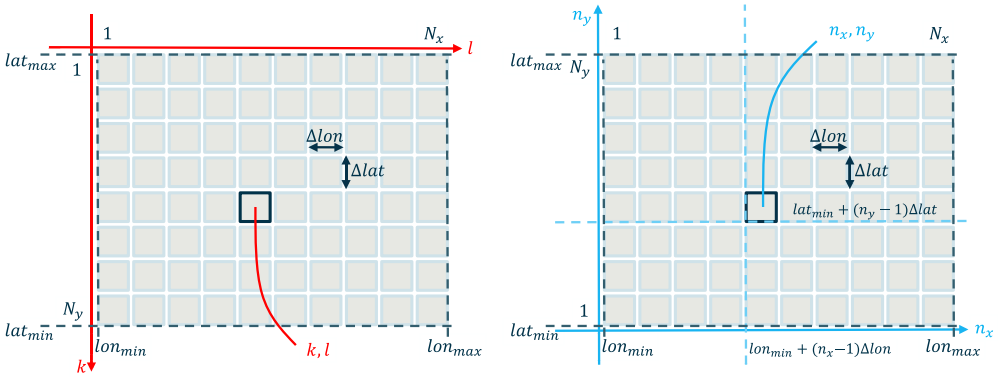

FIGURE 1. User traffic grid conversion.

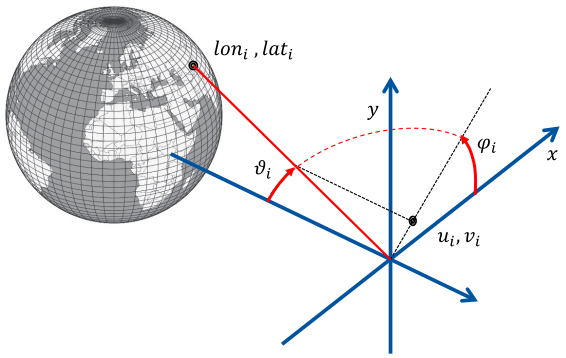

FIGURE 2. Satellite geometry.

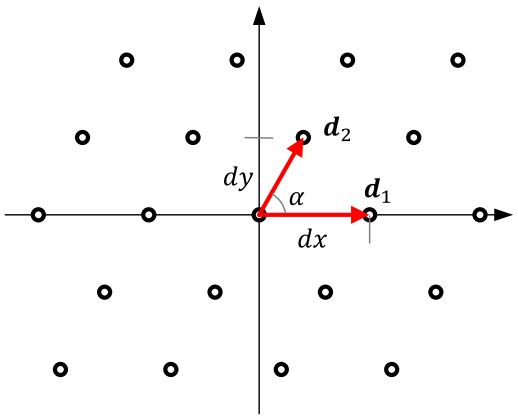

FIGURE 3. Array lattice geometry.

The on-board active antenna can be modelled as a planar array composed of N_T radiating elements placed on a periodic lattice. In the following we adhere to the notation described in [27]. Planar periodic lattices can be identified (non-uniquely) by two linearly independent base vectors, $\boldsymbol{d}_1$ and $\boldsymbol{d}_2$

$$\boldsymbol{d}_1 = \begin{bmatrix} d_{1x} \\ d_{1y} \end{bmatrix}, \ \boldsymbol{d}_2 = \begin{bmatrix} d_{2x} \\ d_{2y} \end{bmatrix}, \tag{15}$$

which can be arranged into a lattice base matrix $\boldsymbol{D}$

$$\boldsymbol{D} = \left[\boldsymbol{d}_1, \boldsymbol{d_2}\right]. \tag{16}$$

The set of all linear combinations of the base vectors $\boldsymbol{d}_1, \boldsymbol{d_2}$ with integer coefficients defines the bi-dimensional lattice $\Lambda(\boldsymbol{D})$. Any point of the lattice, $\boldsymbol{r}_n$, is the superposition of integer multiples of the basis vectors $\boldsymbol{d}_1, \boldsymbol{d_2}$

$$\boldsymbol{r}_n = \boldsymbol{D}\boldsymbol{n} = \boldsymbol{D}\begin{bmatrix} n_1 \\ n_2 \end{bmatrix} = n_1\boldsymbol{d}_1 + n_2\boldsymbol{d_2}. \tag{17}$$

Without loss of generality,[4] we can consider the periodic lattice organized in rows ($d_{1y} = 0$), according to the geometry shown in Fig. 3. With this choice the lattice base matrix $\boldsymbol{D}$ is upper triangular and is parameterized by the three quantities:

- dx, horizontal spacing of elements within the same row;
- dy, vertical spacing of rows;
- α, lattice skew angle.

$$\boldsymbol{D} = \begin{bmatrix} dx & dy\cot\alpha \\ 0 & dy \end{bmatrix}. \tag{18}$$

Two elementary lattice geometries have been used for the array layout, the square lattice and the equilateral triangular lattice

$$\boldsymbol{D}_{\text{SQU}} = dx\begin{bmatrix} 1 & 0 \\ 0 & 1 \end{bmatrix} \quad ; \quad \boldsymbol{D}_{\text{TRI}} = dx\begin{bmatrix} 1 & \frac{\sqrt{3}}{2} \\ 0 & 1 \end{bmatrix}. \tag{19}$$

Assuming the lattice base matrix $\boldsymbol{D}$ normalized to the wavelength λ_w (being $\lambda_w = f_0/c_l$ the free-space wavelength, f_0 the carrier frequency and c_l the speed of light), the bi-dimensional Fourier transform of the periodic lattice in the direct space $\Lambda(\boldsymbol{D})$ produces a dual lattice $\Lambda(\boldsymbol{G})$ in the (u, v) space with a lattice base matrix $\boldsymbol{G}$ given by

$$\boldsymbol{G} = (\boldsymbol{D}^{-1})^T. \tag{20}$$

For a uniform excitation of the array, the lattice $\Lambda(\boldsymbol{G})$ corresponds to the periodic lattice of the main-lobe and all grating lobes in the (u, v) space. The relationship between the periodic lattice in the direct space and the grating lobes'

[4]Solid rotation of the array geometry as well as any affine deformation of it can be considered trivial extensions of the considered geometry [28].

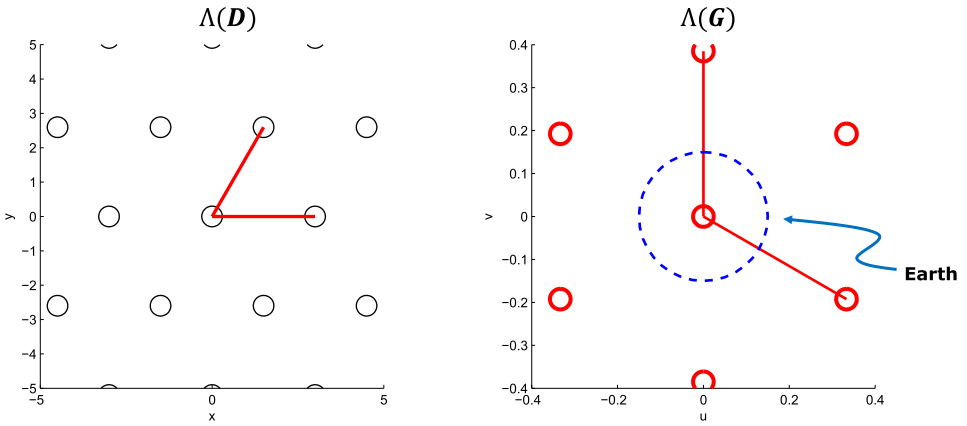

FIGURE 4. Element lattice $\Lambda(\boldsymbol{D})$, and grating-lobes Lattice $\Lambda(\boldsymbol{D})$.

lattice in the far-field space is exemplified in Fig. 4 for an equilateral triangular lattice of elements spaced $3\lambda_w$.

An automated procedure for the generation of the set of array elements positions $\{\boldsymbol{r}_n\,,\ n=1,\cdots,N_T\}$ has been implemented that takes as input parameters:

- the lattice base matrix $\boldsymbol{D}$, see (18);
- a binary flag identifying whether the array lattice is centered in (0, 0) or displaced to a lattice cell centroid[5];
- the parameters defining the rim of the array as a regular polygon:
  - the diameter of the polygonal rim (corresponding to the diameter of the circumscribing circle);
  - the number of edges (assuming the regular polygonal rim to be inscribed in the circumscribing circle);
  - the angle of a first vertex of the polygonal rim (in counter-clock direction from the x-axis).

The procedure, graphically shown in Fig. 5, is based on a number of steps:

- the Array Rim is defined from the regular polygon parameters;
- the regular polygon identifies a Circumscribing Circle;
- a Tangential Rhombus (with edges parallel to the basis vectors $\boldsymbol{d}_1, \boldsymbol{d_2}$) inscribing the circumscribing circle of the regular polygonal rim is defined;
- an Integer Rhombus is obtained rounding the Tangential Rhombus to the nearest integer points (still with edges parallel to $\boldsymbol{d}_1, \boldsymbol{d_2}$);
- a rectangular grid of elements (Generated Points) is generated and distorted by the lattice base matrix $\boldsymbol{D}$ to cover the Integer Rhombus;
- the retained Array Elements correspond to he Generated Points with coordinates within the Array Rim polygon;
- N_T is derived counting the number of Array Elements.

An advantage of the devised procedure stands in the limited over-sizing of the discrete set of elements to be generated for being tested in terms of belonging to the array aperture.

[5]This is useful for obtaining even number of rows or columns; $\boldsymbol{r}_n = \boldsymbol{D}\boldsymbol{n} + \boldsymbol{d}_0, \boldsymbol{d}_0 = \frac{1}{2}\boldsymbol{D}\,[1,\,1]^T$.

Assuming that all the radiating elements are identical and equally oriented in space with a common element radiation pattern $g_E(\vartheta,\phi)$, using the far-field approximation [29], we can obtain the co-polar radiation pattern as

$$g(\vartheta,\phi) = g_E(\vartheta,\phi)\sum_{n=1}^{N_T} w_n \cdot \exp\left[jk_0(x_n\sin\vartheta\cos\phi + y_n\sin\vartheta\sin\phi)\right], \quad (21)$$

where w_n corresponds to the complex excitation coefficient of the n-th array element. Introducing the vectorial notation for the normalized n-th element position, $\boldsymbol{r}_n = x_n\hat{\boldsymbol{x}} + y_n\hat{\boldsymbol{y}}$, and for the (u, v) look direction, $\boldsymbol{u} = u\hat{\boldsymbol{x}} + v\hat{\boldsymbol{y}}$, (21) can be rewritten as

$$g(\boldsymbol{u}) = g_E(\boldsymbol{u})\sum_{n=1}^{N_T} w_n \exp\left(j2\pi\,\boldsymbol{u}\cdot\boldsymbol{r}_n\right). \quad (22)$$

A simple rotationally symmetric element radiation pattern [30] is used in the modelling

$$g_E(\vartheta) = \sqrt{G_E^{\max}}\cos^{q_E}(\vartheta),\quad \begin{aligned} G_E^{\max} &= 4\pi A_E 10^{\frac{\eta_E(dB)}{10}},\\ q_E &= \tfrac{1}{4}G_E^{\max} - \tfrac{1}{2}, \end{aligned} \quad (23)$$

where $G_E^{\max}$ is the peak gain of the radiating element, A_E is the Direct Radiating Array (DRA) elementary cell area normalised to the wavelength squared, and $\eta_E(dB)$ is the radiating element efficiency expressed in dB. Assuming $\boldsymbol{D}$ normalised to the wavelength, the elementary cell area can be determined by as

$$A_E = \det(\boldsymbol{D}) = dx\,dy\,. \quad (24)$$

Exact evaluation of the array gain would entail an additional corrective factor involving the integration of (22) on the whole sphere. While analytical results exists the for planar arrays with the element pattern defined by (23) [31], the direct use of use (22) is sufficiently accurate for large antenna elements ($dx > 2\lambda_w$).

The H-RRM performance improvement exploiting the enhanced active antenna model is testified by the simulation results reported in Sec. IV-D.

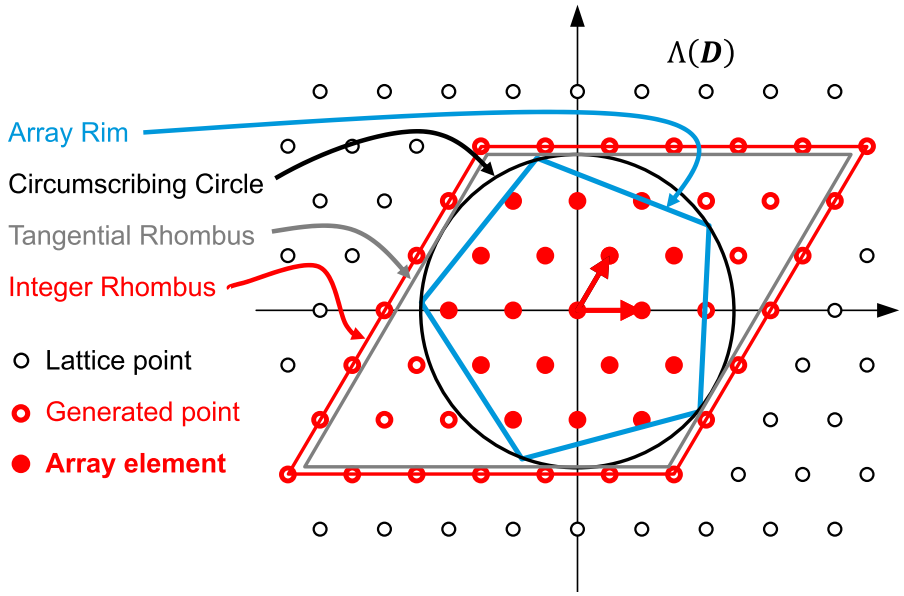

FIGURE 5. Array construction.

C. CHANNEL STATE INFORMATION ESTIMATION ERROR IMPACT

So far all the M-MIMO MMSE precoding results reported in [12] and [17] have assumed a perfect channel estimation. It is interesting to assess the impact on the possible estimation error on the MMSE pre-coding performance as literature results so far have been mainly related to the single feed per beam case [3]. To do so we have extended the M-MIMO channel model to include random phase and amplitude errors in each element of the estimated channel matrix $\mathbf{H}$. The ideal channel matrix $\mathbf{H}$ is then replaced by the estimated channel matrix $\hat{\mathbf{H}}$ with its elements $\hat{h}_{i,j}$ computed as

$$\hat{h}_{i,j} = h_{i,j} 10^{\frac{\Delta A_{i,j}^{dB}}{10}} \exp\left(\jmath \frac{\pi}{180} \Delta\varphi_{i,j}^{deg}\right), \tag{25}$$

where $\Delta A_{i,j}^{dB}$ and $\Delta\varphi_{i,j}^{deg}$ are random variables representing the realizations of the amplitude and phase channel estimate errors expressed in degrees and dB.

Simulation results in the presence of channel estimation errors for MMSE precoding are shown in Sec. IV-E.

D. TRAFFIC REQUEST SATISFACTION ANALYSIS

To better appreciate the system capability to serve the non uniform traffic request over the coverage region we have been partitioning the coverage region in squared areas (“pixels”) with programmable granularity and computing the requested and provided throughput for each pixel. In this way it is possible to appreciate the effective spatial throughput performance of the system on top of the aggregated performance reported in the tables above. By introducing this spatial coverage area partitioning, it is possible to assess the system capability to satisfy the traffic demand in each pixel[6] $\mathbb{P}_l$ with $l = 1, \cdots N_{px}$. For this purpose we introduce the concept of per pixel spatial and total traffic throughput request $T_R(l)$, T_R^{TOT} and per pixel or total raw throughput offer $T_O(l)$, T_O^{TOT} defined as

$$T_R(l) = \iint_{(x,y)\in\mathbb{P}_l} t_R(x,y)\, dxdy, \quad T_R^{TOT} = \sum_{l=1}^{N_{px}} T_R(l), \tag{26}$$

$$T_O(l) = \iint_{(x,y)\in\mathbb{P}_l} t_O(x,y)\, dxdy, \quad T_O^{TOT} = \sum_{l=1}^{N_{px}} T_O(l), \tag{27}$$

where $t_R(x,y)$ and $t_O(x,y)$ represent respectively the traffic throughput request and offered spatial distribution over the coverage area in Gbps/m^2. Clearly $T_R(l)$ and $T_O(l)$ are expressed in Gbps/pixel while T_R^{TOT} and T_O^{TOT} are measured in Gbps. The useful throughput per pixel and total correspond to

$$T_U(l) = \min\left\{T_R(l),\ T_O(l)\right\}, \quad T_U^{TOT} = \sum_{l=1}^{N_{px}} T_U(l). \tag{28}$$

Finally, the per pixel and total delta throughput offered versus requested traffic can then simply computed as

$$T_\Delta(l) = T_O(l) - T_R(l), \quad T_\Delta^{TOT} = \sum_{l=1}^{N_{px}} T_\Delta(l). \tag{29}$$

A concise way to express the system capability to comply with the non uniform traffic request is to use the traffic satisfaction factor defined as $S_{TR} = T_U^{TOT}/T_R^{TOT}$.

[6]It is worth noting that the definition of the size of these throughput “pixels” is independent from that of the traffic histogram pixels.

In the following simulations, the total amount of traffic request is sized to the raw throughput available in a given system configuration for the current M-MIMO scheme adopted i.e.: a) Matched Filter (MF), b) MMSE M-MIMO, c) Multi-Beam (MB) or d) MB plus Quasi-Virtual Distancing (MB+QVD) pragmatic M-MIMO. By raw throughput we consider the throughput provided by the system irrespective of its matching with the capacity request distribution. For a given set of system parameters the raw throughput, and hence the amount of requested traffic, is then depending on the actual average number of active users represented by N_U. The total traffic request T_R^{TOT}, equal to the raw system throughput, is then distributed over the pixels according to the estimated discrete traffic normalized distribution $T_R(l)/T_R^{TOT}$.

The traffic request satisfaction factors introduced above is extensively exploited for optimizing the system operating point as discussed in Sec. IV-F.

IV. NUMERICAL RESULTS AND DISCUSSION

A. COMPARISON OF TDM AND FDM FOR M-MIMO AND H-RRM

Following the results of section II-A, we have been extending the simulator developed in [17] to cover the FDM case. To validate the simulator we have been repeating the throughput simulations for the various traffic configurations (uniform and not uniform) obtaining the same results as the ones reported in Sec. IV of [17]. These simulation findings are not repeated here for sake of brevity, validate the M-MIMO H-RRM TDM/FDM perfect duality.

B. MMSE PRECODING LAGRANGE MULTIPLIER OPTIMIZATION

Following Sec. II-B Lagrange multiplier optimization findings, it was apparent the need to repeat the MMSE simulation results for the cases reported in [17]. So the M-MIMO with H-RRM system simulator was modified to include (6-7). It should be recalled that the MMSE precoding throughput results assume ideal channel state estimation. This means that no other impairments due to real-life aspects (e.g. channel estimation, users multiplexing on the same frame, multiple gateways…) while MB and MB+QVD throughput are representing truly realistic performance results.

The new simulation findings for a 1.2 m DRA size are summarized in Table 1 for Shannon throughput and in Table 2 for DVB-S2X throughput. When comparing these new results to the ones reported in Tables 4-5 in [17], it is apparent that the MMSE performance with optimized Lagrange multiplier is considerably better for the cases where traffic is limited to a small percentage of the satellite coverage area i.e cases 2c, 3c, 2d, 3d, 2e, 3e, 2f, 3f. The bigger gain is for cases 3c, 3d, 3e, 3f whereby the traffic area S_T is in the range 8-16% of the overall satellite coverage area S_A (see Sec. II.C and Table 1 in [17] for its definition and numerical evaluation). In this case the MMSE throughput advantage vs MB+QVD is in the range 40-45% instead of 10-12% without Lagrange multiplier optimization. For cases 2c, 2d, 2e, 2f the traffic area S_T is in the range 20-40% of the overall satellite coverage area S_A. In this case the MMSE throughput advantage vs MB+QVD is in the range 31-36% instead of 12-13% without Lagrange multiplier optimization. Instead for cases 2a, 2b the MMSE throughput advantage vs MB+QVD is 11-12% compared to 8%. For cases 0 and 1 corresponding to an uniform traffic Poisson Point and Poisson Disc distribution respectively, as expected, the difference is found to be negligible.

The new simulation 2.0 m DRA findings are summarized in Table 3 for Shannon throughput and in Table 4 for

TABLE 1. Shannon throughput results for traffic cases 0-3 with H-RRM and optimized Lagrange multiplier, $D_A = 1.2$ m, non even traffic spot distribution for cases 2-3, $C = 30$.

Case	Predicted $\left[\frac{N_T}{N_U}\right]_{opt}$	Simulated $\left[\frac{N_T}{N_U}\right]_{opt}$	Shannon Throughput (Gbps) / Δ vs MB+QVD %			
			MF	MB	MB+QVD	MMSE
0	NA	2.0	3.70E+02 +2.3	3.62E+02 -0.2	3.62E+02 0.0	3.87E+02 +6.9
1	NA	2.2	3.22E+02 +1.0	3.15E+02 -1.0	3.18E+02 0.0	3.56E+02 +12.0
2a	2.4	2.4	2.22E+02 +2.8	2.18E+02 +1.0	2.16E+02 0.0	2.43E+02 +12.2
2b	2.4	2.4	2.34E+02 +2.7	2.30E+02 +0.9	2.28E+02 0.0	2.54E+02 +11.6
2c	9.9	10.0	1.23E+02 -2.8	1.21E+02 -4.5	1.26E+02 0.0	1.66E+02 +30.9
2d	12.0	12.0	1.01E+02 -2.2	9.91E+01 -3.9	1.03E+02 0.0	1.40E+02 +35.7
2e	8.0	8.0	1.26E+02 -0.4	1.23E+02 -2.1	1.26E+02 0.0	1.66E+02 +31.6
2f	6.0	7.0	1.40E+02 +0.1	1.38E+02 -1.6	1.40E+02 0.0	1.80E+02 +28.3
3a	4.1	4.1	1.98E+02 +0.9	1.94E+02 -0.9	1.96E+02 0.0	2.31E+02 +18.0
3b	4.1	4.1	2.12E+02 +0.1	2.08E+02 -1.7	2.12E+02 0.0	2.48E+02 +17.4
3c	23.7	22.0	5.96E+01 -5.5	5.86E+01 -7.1	6.30E+01 0.0	8.87E+01 +40.6
3d	28.6	28.0	4.83E+01 -4.3	4.75E+01 -5.9	5.05E+01 0.0	7.35E+01 +45.5
3e	19.1	20.0	6.22E+01 -2.6	6.12E+01 -4.2	6.38E+01 0.0	9.08E+01 +42.3
3f	14.3	15.0	7.37E+01 -1.4	7.25E+01 -3.1	7.47E+01 0.0	1.04E+02 +39.1

TABLE 2. DVB-S2X throughput results for traffic cases 0-3 with H-RRM and optimized Lagrange multiplier, $D_A = 1.2$ m, non even traffic spot distribution for cases 2-3, $C = 30$.

Case	Predicted $\left[\frac{N_T}{N_U}\right]_{opt}$	Simulated $\left[\frac{N_T}{N_U}\right]_{opt}$	DVB-S2X Throughput (Gbps) / Δ vs MB+QVD %			
			MF	MB	MB+QVD	MMSE
0	NA	2.0	3.03E+02 +2.5	2.95E+02 -0.3	2.96E+02 0.0	3.14E+02 +6.0
1	NA	2.2	2.61E+02 +1.2	2.55E+02 -1.0	2.57E+02 0.0	2.88E+02 +11.7
2a	2.4	2.4	1.66E+02 +2.9	1.62E+02 +0.9	1.61E+02 0.0	1.82E+02 +12.9
2b	2.4	2.4	1.75E+02 +3.1	1.71E+02 +0.7	1.70E+02 0.0	1.90E+02 +12.0
2c	9.9	10.0	1.01E+02 -2.9	9.88E+01 -4.7	1.04E+02 0.0	1.37E+02 +32.4
2d	12.0	12.0	8.26E+01 -2.1	8.11E+01 -3.9	8.43E+01 0.0	1.16E+02 +37.5
2e	8.0	8.0	1.01E+02 -0.4	9.93E+01 -2.2	1.02E+02 0.0	1.37E+02 +35.2
2f	6.0	7.0	1.12E+02 +0.2	1.10E+02 -1.7	1.12E+02 0.0	1.49E+02 +32.4
3a	4.1	4.1	1.55E+02 +0.9	1.52E+02 -1.0	1.54E+02 0.0	1.84E+02 +19.7
3b	4.1	4.1	1.68E+02 +0.1	1.65E+02 -1.9	1.68E+02 0.0	1.99E+02 +18.4
3c	23.7	22.0	4.89E+01 -5.6	4.80E+01 -7.3	5.18E+01 0.0	7.49E+01 +44.6
3d	28.6	28.0	3.98E+01 -4.3	3.91E+01 -6.0	4.16E+01 0.0	6.24E+01 +49.9
3e	19.1	20.0	5.10E+01 -2.6	5.01E+01 -4.2	5.23E+01 0.0	7.63E+01 +45.9
3f	14.3	15.0	6.02E+01 -1.4	5.91E+01 -3.2	6.10E+01 0.0	8.67E+01 +42.0

TABLE 3. Shannon throughput results for traffic cases 0-3 with H-RRM and optimized Lagrange multiplier, $D_A = 2.0$ m, non even traffic spot distribution for cases 2-3, $C = 30$.

Case	Predicted $\left[\frac{N_T}{N_U}\right]_{opt}$	Simulated $\left[\frac{N_T}{N_U}\right]_{opt}$	Shannon Throughput (Gbps) / Δ vs MB+QVD %			
			MF	MB	MB+QVD	MMSE
0	NA	2.0	9.82E+02 +2.4	9.57E+02 -0.1	9.58E+02 0.0	1.02E+03 +6.5
1	NA	2.2	8.63E+02 +0.9	8.45E+02 -1.1	8.55E+02 0.0	9.56E+02 +11.8
2a	2.4	2.4	6.02E+02 +2.4	5.92E+02 +0.6	5.88E+02 0.0	6.51E+02 +10.7
2b	2.4	2.4	6.25E+02 +2.4	6.14E+02 +0.6	6.11E+02 0.0	6.74E+02 +10.4
2c	9.9	10.0	3.16E+02 -2.3	3.11E+02 -4.0	3.24E+02 0.0	4.20E+02 +29.8
2d	12.0	12.0	2.56E+02 -1.3	2.51E+02 -3.0	2.59E+02 0.0	3.46E+02 +33.5
2e	8.0	8.0	3.28E+02 -0.4	3.22E+02 -2.1	3.29E+02 0.0	4.22E+02 +28.2
2f	6.0	7.0	3.67E+02 +0.1	3.61E+02 -1.6	3.66E+02 0.0	4.61E+02 +25.8
3a	4.1	4.1	5.27E+02 +0.6	5.17E+02 -1.2	5.24E+02 0.0	6.11E+02 +16.7
3b	4.1	4.1	5.58E+02 0.0	5.48E+02 -1.8	5.58E+02 0.0	6.52E+02 +16.7
3c	23.7	22.0	1.49E+02 -4.1	1.46E+02 -5.8	1.55E+02 0.0	2.15E+02 +38.9
3d	28.6	28.0	1.18E+02 -3.4	1.16E+02 -5.1	1.22E+02 0.0	1.75E+02 +43.5
3e	19.1	20.0	1.58E+02 -2.3	1.56E+02 -3.7	1.62E+02 0.0	2.24E+02 +38.6
3f	14.3	15.0	1.87E+02 -0.9	1.83E+02 -2.7	1.88E+02 0.0	2.54E+02 +34.9

TABLE 4. DVB-S2X throughput results for traffic cases 0-3 with H-RRM, $D_A = 2.0$ m and optimized Lagrange multiplier, non even traffic spot distribution for cases 2-3, $C = 30$.

Case	Predicted $\left[\frac{N_T}{N_U}\right]_{opt}$	Simulated $\left[\frac{N_T}{N_U}\right]_{opt}$	DVB-S2X Throughput (Gbps) / Δ vs MB+QVD %			
			MF	MB	MB+QVD	MMSE
0	NA	2.0	8.06E+02 +3.4	7.80E+02 0.0	7.80E+02 0.0	8.37E+02 +7.3
1	NA	2.2	6.98E+02 +1.0	6.83E+02 -1.1	6.91E+02 0.0	7.73E+02 +11.8
2a	2.4	2.4	4.48E+02 +2.6	4.39E+02 +0.5	4.37E+02 0.0	4.87E+02 +11.6
2b	2.4	2.4	4.63E+02 +2.7	4.53E+02 +0.5	4.51E+02 0.0	4.99E+02 +10.8
2c	9.9	10.0	2.57E+02 -2.5	2.52E+02 -4.3	2.64E+02 0.0	3.47E+02 +31.8
2d	12.0	12.0	2.10E+02 -1.5	2.06E+02 -3.2	2.13E+02 0.0	2.87E+02 +34.6
2e	8.0	8.0	2.63E+02 -0.4	2.58E+02 -2.3	2.64E+02 0.0	3.47E+02 +31.5
2f	6.0	7.0	2.94E+02 +0.2	2.88E+02 -1.7	2.93E+02 0.0	3.80E+02 +29.7
3a	4.1	4.1	4.13E+02 +0.7	4.05E+02 -1.3	4.10E+02 0.0	4.85E+02 +18.3
3b	4.1	4.1	4.43E+02 -0.1	4.34E+02 -2.1	4.44E+02 0.0	5.23E+02 +17.8
3c	23.7	22.0	1.22E+02 -4.0	1.19E+02 -5.8	1.27E+02 0.0	1.80E+02 +42.2
3d	28.6	28.0	9.66E+01 -3.6	9.48E+01 -5.4	1.00E+02 0.0	1.48E+02 +47.5
3e	19.1	20.0	1.29E+02 -2.3	1.27E+02 -3.8	1.32E+02 0.0	1.88E+02 +42.0
3f	14.3	15.0	1.51E+02 -0.9	1.48E+02 -2.8	1.52E+02 0.0	2.10E+02 +37.8

DVB-S2X throughput. When comparing these new results to the ones reported in Tables 4-5 in [17], it is apparent that, as for the smaller array case, the MMSE performance with optimized Lagrange multiplier is better for the cases where traffic is limited to a small percentage of the satellite coverage area i.e cases 2-3c, 2-3d, 2-3e, 2-3f. The bigger gain is for case 3c, 3d, 3e, 3f whereby the traffic area S_T is in the range 8-16% of the overall satellite coverage area S_A. In this case the MMSE throughput advantage vs MB+QVD is in the range 35-43% instead of 23-27% without Lagrange multiplier optimization. For cases 2c, 2d, 2e, 2f the traffic area S_T is in the range 20-40% of the overall satellite coverage area S_A. In this case the MMSE throughput advantage vs MB+QVD is in the range 26-30% instead of 22-23% without Lagrange multiplier optimization. Instead for cases 2a and 2b the MMSE throughput advantage vs MB+QVD is comparable to the non optimized case. For cases 3a and 3b the MMSE throughput advantage vs MB+QVD is just 1% higher than what reported in [17]. For cases 0 and 1 the difference is also negligible. Some simulation for larger DRA size (3 m) has also been performed showing a further reduction in the MMSE performance gap vs MB+QVD.

We can conclude that for array larger or equal than 2 m the Lagrange multiplier optimization impact is quite marginal.

C. EXTENDED GRIDDED POPULATION OF THE WORLD DATABASE

For the following analyses the input tabular histograms of the traffic demand have been derived according to the forecasting methodology described in [25]. The methodology is based on the merging of three sources of traffic demand:

- The population density for consumer broadband (derived from Gridded Population of the World database - GPW [26], and weighed by an addressable market factor);
- the maritime vessel distribution;
- the airplanes traffic distribution.

The resulting tabular histogram shown in Fig. 6 dubbed Extended Gridded Population of the World database (E-GPW), is defined on a world map with grid cells of $\Delta_{lon} = 0.25° \times \Delta_{lat} = 0.25°$ lon-lat resolution, and can be used to generate random user locations according to the method reported in Sect. III-A. Figure 7 provides an example of world-wide generation of $N_U = 10000$ users. In practical cases, one may be interested in generating users in a satellite limited field-of-view, or according to some other restriction (e.g. minimum elevation angle, continental distribution, commercial target area, etc.). For this purpose, the tabular histogram can be pre-filtered nulling the cells outside the area of interest and then the inversion sampling is applied. This approach has the advantage of allowing a direct generation of an assigned number of users without recurring to trial-and-error generation/rejection techniques.

D. REFINED ACTIVE ANTENNA MODEL FOR H-RRM

Tables 5 and 6 are providing simulation results when adopting the more accurate active antenna model described in Sec. III-B with circular rim and radiating elements on an equilateral triangular lattice. We selected the 2.0 m DRA size being the most interesting case. We observe that the adoption of a more accurate direct radiating array antenna model provides an improvement of the M-MIMO performance which is definitely more marked for the MF, MB, MB+QVD techniques compared to MMSE. This can be explained by the fact that the MMSE is more resistant to co-channel interference than the other techniques. It is also

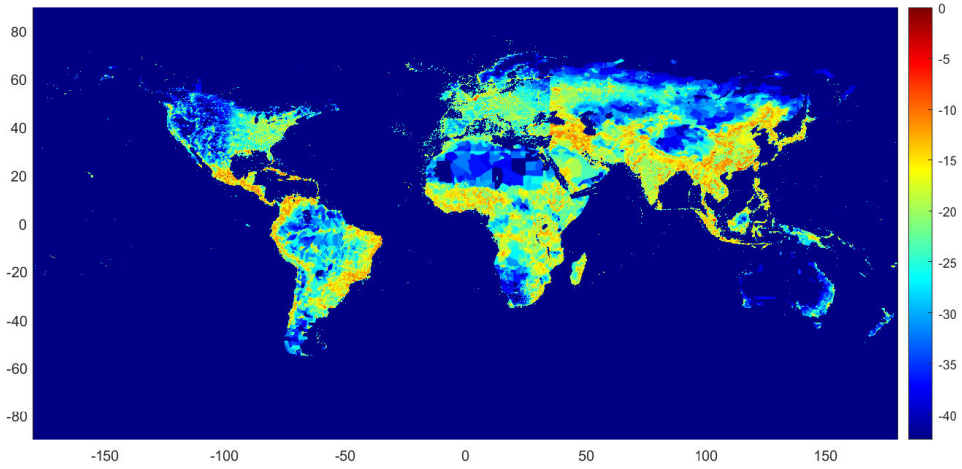

FIGURE 6. Normalized E-GPW traffic demand [dB].

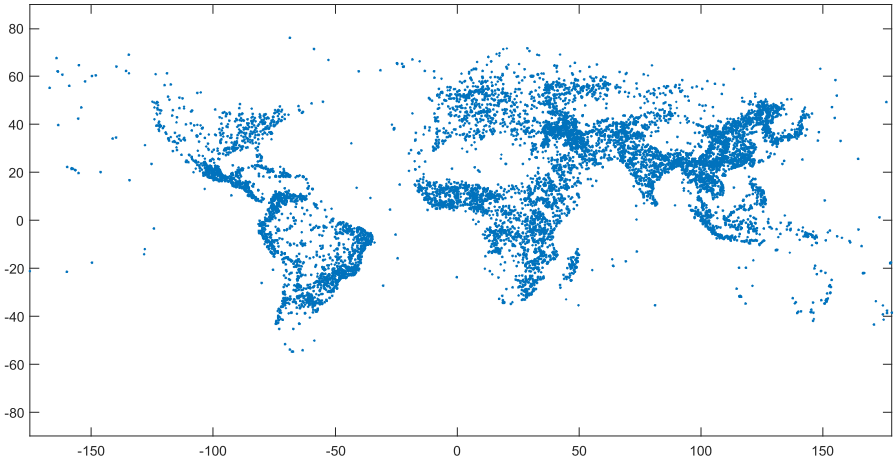

FIGURE 7. E-GPW random user generation realization for 10000 users.

remarked that the performance improvement is more pronounced for the Case 3 corresponding to a traffic limited to a small percentage of the coverage area. In particular for the case 3d the MB+QVD Shannon throughput performance gap compared to MMSE amounts to 31.4 % compared to the 43.5 % found with the simplified antenna model, thus a 12 % improvement (see Table 3 results). In the milder (in terms of traffic area over coverage area ratio) 2d case the the MB+QVD Shannon throughput performance gap compared to MMSE amounts to 25.8 % compared to the 33.5 % found with the simplified antenna model. Instead when the traffic is present over the full coverage region (see cases 2a/b) the improvement is reduced to 2.4 %.

We can conclude that a more accurate antenna model for H-RRM is beneficial for all considered cases, but more pronounced for pragmatic M-MIMO techniques (MB and MB+QVD). The improvement is more significant when the traffic is concentrated on a fraction of the satellite coverage area.

E. CHANNEL STATE INFORMATION ESTIMATION ERROR

For simplicity we assume an uniform phase in the range $\pm\Delta\varphi_{max}^{deg}$) and amplitude ($\pm\Delta A_{max}^{dB}$) error distribution respectively. Simulation results with $\Delta\varphi_{max}^{deg} = 15$ degrees and $\Delta A_{max}^{dB} = 2$ dB for the previously analysed configuration indicate no appreciable throughout performance impact. These assumptions are representative of locally calibrated active antenna radio frequency chains differential errors. It is recalled that, in practice, the per antenna element channel estimation on ground is impossible due to the very low SNIR values that will be observed. Therefore, the payload differential channel errors can only be corrected through on-board techniques [32]. Further simulations results for the American regional coverage study case, confirming what stated above, are reported in Sec. IV-F.

This finding can be explained by the fact that the dominant effect affecting the M-MIMO performance is the satellite antenna pattern rather than the individual array elements amplitude and phase errors.

TABLE 5. Shannon throughput results for traffic cases 0-3 with H-RRM, optimized Lagrange multiplier and refined active antenna model, $D_A = 2.0$ m, non even traffic spot distribution for cases 2-3, $C = 30$.

Case	Predicted $\left[\frac{N_T}{N_U}\right]_{opt}$	Simulated $\left[\frac{N_T}{N_U}\right]_{opt}$	Shannon Throughput (Gbps) / Δ vs MB+QVD %			
			MF	MB	MB+QVD	MMSE
0	NA	2.0	9.82E+02 +2.4	9.57E+02 -0.1	9.58E+02 0.0	1.02E+03 +6.5
1	NA	2.2	8.63E+02 +0.9	8.45E+02 -1.1	8.55E+02 0.0	9.56E+02 +11.8
2a	2.4	2.4	6.22E+02 +2.0	6.10E+02 -0.1	6.10E+02 0.0	6.60E+02 +8.2
2b	2.4	2.4	6.48E+02 +2.1	6.36E+02 +0.1	6.35E+02 0.0	6.86E+02 +8.0
2c	9.9	10.0	3.45E+02 -1.7	3.36E+02 -4.1	3.51E+02 0.0	4.31E+02 +22.8
2d	12.0	12.0	2.78E+02 -0.8	2.71E+02 -3.1	2.80E+02 0.0	3.53E+02 +25.8
2e	8.0	8.0	3.53E+02 +0.4	3.45E+02 -1.8	3.51E+02 0.0	4.30E+02 +22.5
2f	6.0	7.0	3.95E+02 +0.3	3.86E+02 -2.0	3.94E+02 0.0	4.74E+02 +20.2
3a	4.1	4.1	5.27E+02 +0.6	5.17E+02 -1.2	5.24E+02 0.0	6.11E+02 +16.7
3b	4.1	4.1	5.95E+02 +0.4	5.82E+02 -1.9	5.93E+02 0.0	6.67E+02 +12.5
3c	23.7	22.0	1.67E+02 -2.9	1.62E+02 -5.5	1.72E+02 0.0	2.18E+02 +27.2
3d	28.6	28.0	1.32E+02 -2.1	1.29E+02 -4.7	1.35E+02 0.0	1.77E+02 +31.4
3e	19.1	20.0	1.74E+02 -1.1	1.69E+02 -3.7	1.76E+02 0.0	2.27E+02 +29.4
3f	14.3	15.0	2.04E+02 -0.4	1.99E+02 -2.7	2.05E+02 0.0	2.61E+02 +27.2

TABLE 6. DVB-S2X throughput results for traffic cases 0-3 with H-RRM, $D_A = 2.0$ m, optimized Lagrange multiplier and refined active antenna model, non even traffic spot distribution for cases 2-3, $C = 30$.

Case	Predicted $\left[\frac{N_T}{N_U}\right]_{opt}$	Simulated $\left[\frac{N_T}{N_U}\right]_{opt}$	DVB-S2X Throughput (Gbps) / Δ vs MB+QVD %			
			MF	MB	MB+QVD	MMSE
0	NA	2.0	8.06E+02 +3.4	7.80E+02 0.0	7.80E+02 0.0	8.37E+02 +7.3
1	NA	2.2	6.98E+02 +1.0	6.83E+02 -1.1	6.91E+02 0.0	7.73E+02 +11.8
2a	2.4	2.4	4.62E+02 +2.3	4.50E+02 -0.3	4.51E+02 0.0	4.92E+02 +9.0
2b	2.4	2.4	4.79E+02 +2.2	4.69E+02 +0.0	4.69E+02 0.0	5.09E+02 +8.4
2c	9.9	10.0	2.82E+02 -1.9	2.75E+02 -4.4	2.87E+02 0.0	3.56E+02 +23.8
2d	12.0	12.0	2.27E+02 -0.7	2.22E+02 -3.1	2.229E+02 0.0	2.91E+02 +27.2
2e	8.0	8.0	2.87E+02 +0.5	2.80E+02 -1.9	2.85E+02 0.0	3.55E+02 +24.4
2f	6.0	7.0	3.20E+02 +0.4	3.12+02 -2.0	3.18E+02 0.0	3.92E+02 +23.1
3a	4.1	4.1	4.13E+02 +0.7	4.05E+02 -1.3	4.10E+02 0.0	4.85E+02 +18.3
3b	4.1	4.1	4.76E+02 +0.5	4.64E+02 -1.9	4.73E+02 0.0	5.36E+02 +13.3
3c	23.7	22.0	1.37E+02 -3.0	1.33E+02 -5.7	1.41E+02 0.0	1.83E+02 +29.8
3d	28.6	28.0	1.09E+02 -2.1	1.06E+02 -4.9	1.12E+02 0.0	1.50E+02 +34.0
3e	19.1	20.0	1.43E+02 -1.2	1.39E+02 -3.9	1.44E+02 0.0	1.90E+02 +31.9
3f	14.3	15.0	1.66E+02 -0.4	1.62E+02 -2.9	1.67E+02 0.0	2.16E+02 +29.4

This result is triggering the idea to have a pure feed-forward MMSE precoding implementation, i.e. computing offline the antenna Beam Forming Network (BFN) coefficients based on the estimated antenna elements pattern and traffic distribution disregarding channel estimation errors. Clearly this very simplified approach is sub-optimum if the traffic distribution is not matching the expected one. The alternative is to recompute the BFN coefficients on a regular basis to account for traffic distribution evolution. However, this approach implies higher complexity.

TABLE 7. System parameters for the Americas study case.

Parameter	Value	Unit
Target net throughput	500	Gbps
Satellite GEO orbital location	-79.0 East	degrees
Downlink carrier frequency	18.2	GHz
Carriers aggregate baud rate	1900	Mbaud
Total RF carrier power	34.8	dBW
Number of polarizations	2	
Tx circular array size	2.15	m
Tx array lattice	Triangular	
Element aperture loss	3	dB
Tx antenna gain	49	dBi
Number of polarizations	2	
MB beams normalized distance	0.1, 0.2	for H-RRM
DRA Noise Power Ratio	16.0	dB
Adjacent satellite interference	17.0	dB
User terminal G/T	20.6	dB/K
Implementation losses	1.0	dB
ACM implementation margin	1.0	dB

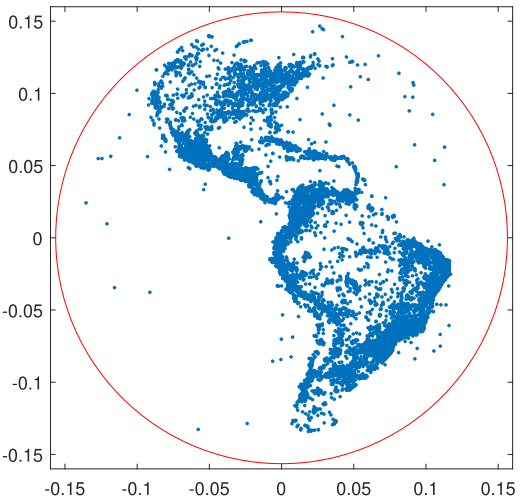

FIGURE 8. Simulated traffic request distribution over the Americas ($N_U = 10000$).

F. SYSTEM STUDY CASE

In this section we look at an hypothetical GEO study case whereby a multi-beam satellite equipped with digital processor, digital beam forming and active antenna is covering the Americas. The main system parameters are summarized in Table 7. As traffic model we adopted the adopted the one described in Sec. III-A. The simulated traffic request distribution in the area of interest is shown in Fig. 8. Making reference to the definitions introduced in Sec. III-D, in this section we will first derive by simulation the raw and useful throughput as well the traffic satisfaction factor as function of the active antenna elements divided by the number of active users (or more precisely carriers) N_T/N_U. This parameter indicates the degree of M-MIMO conditions under which we are operating. Typically for M-MIMO $N_T/N_U \gg 1$ is assumed, although as remarked in [16] this condition is not

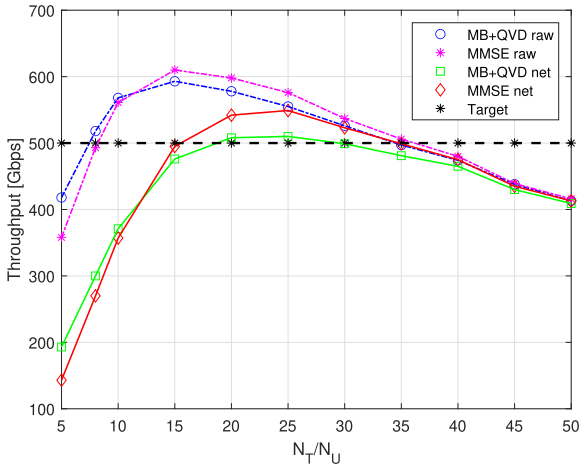

FIGURE 9. Simulated throughput (raw and net) versus N_T/N_U.

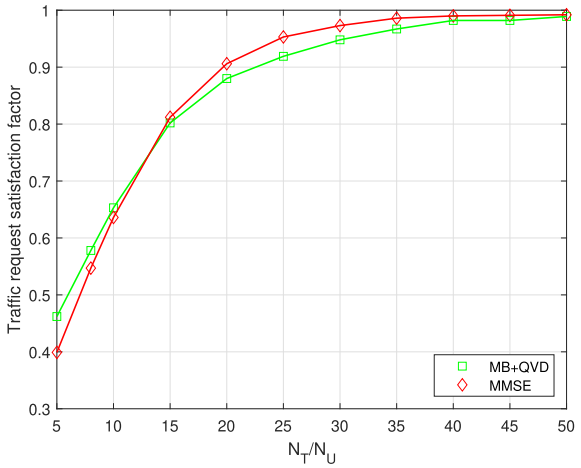

FIGURE 10. Simulated requested traffic satisfaction factor versus N_T/N_U.

a must. To be remarked that throughout the simulations the antenna parameters (e.g. N_T) are fixed. This mean that reducing N_T/N_U we are increasing the system load and vice-versa.

Looking at the simulation results reported in Fig. 9, the optimum value of N_T/N_U maximizing the raw throughput $[N_T/N_U]_{max}$ is different compared to the net throughput. For the latter, the $[N_T/N_U]_{max}$ value for MMSE and MB+QVD is 25. Instead, for the raw throughput the $[N_T/N_U]_{max}$ value for MMSE and MB+QVD is 15. This can be explained by the fact that the MMSE precoding extra co-channel interference mitigation capability allows the system to operate with an higher load (lower N_T/N_U) compared to MB+QVD.

It is remarked that when looking at the achievable system total net throughput without looking at the traffic satisfaction factor, the satellite payload appears slightly oversized for the requested demand, as there is a range of N_T/N_U values for which the requested useful throughput (dash-dotted horizontal line depicted in Fig. 9, the value of which is the net throughput taken from Table 7) is exceeded. For MMSE any N_T/N_U value between 15 and 35 is satisfying the traffic request. Instead, for MB+QVD $18 \leq N_T/N_U \leq 30$ are acceptable values. However, this aggregate useful traffic figure is not revealing the level of spatial traffic satisfaction which will be investigated in the following.

As illustrated in in Sec. III-D, the traffic satisfaction factor is defined as the fraction of the requested traffic served by the system in each coverage region ‘‘pixel’’. In this case, in line with the explanation given in in Sec. III-D, while reducing N_T/N_U we increase the absolute amount of total traffic keeping the defined non-uniform spatial PDF. By doing so we are pushing harder the system, thus reducing the RRM ‘‘space’’ available in the system colors for accommodating the traffic demand in each pixel. We define as optimum system load $[N_T/N_U]_{opt}$, the lowest $[N_T/N_U]$ value achieving the target system throughput with the highest traffic satisfaction factor. In Fig. 9, this corresponds to the leftmost $[N_T/N_U]$ value for which the simulated net system throughput line crosses the target throughput dashed line. Although beyond

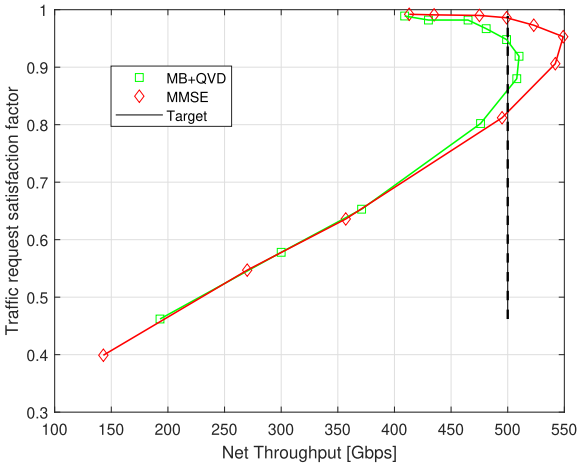

FIGURE 11. Simulated requested traffic satisfaction factor versus the net throughput.

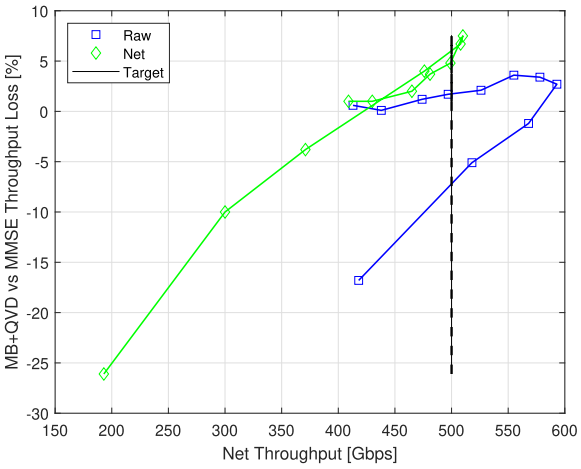

FIGURE 12. Simulated MB+QVD w.r.t. MMSE throughput loss versus the net throughput.

the $[N_T/N_U]_{opt}$ value the net throughput is reduced, the ratio between raw and useful traffic is approaching one. As a consequence, by definition, also the traffic request satisfaction is also approaching the unit value. This happens because

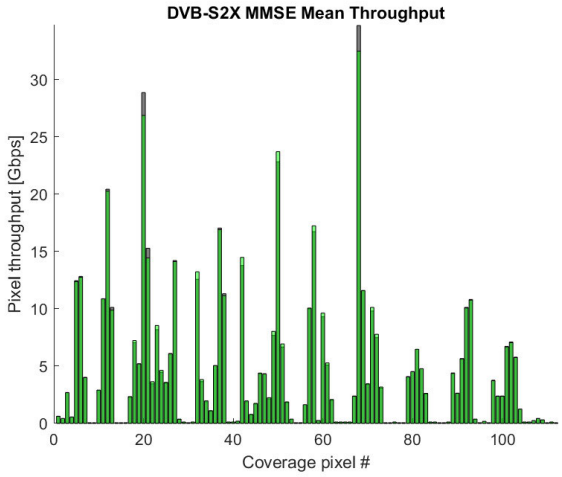

(a) MMSE throughput per pixel for the optimized load value $N_T/N_U = 35$.

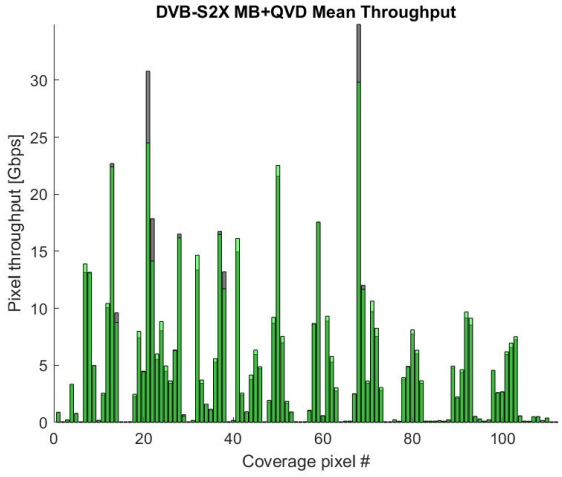

(b) MB+QVD throughput per pixel for the optimized load value $N_T/N_U = 30$.

FIGURE 13. Simulated throughput versus traffic request per coverage pixels, corresponding to the useful throughput matching the target one.

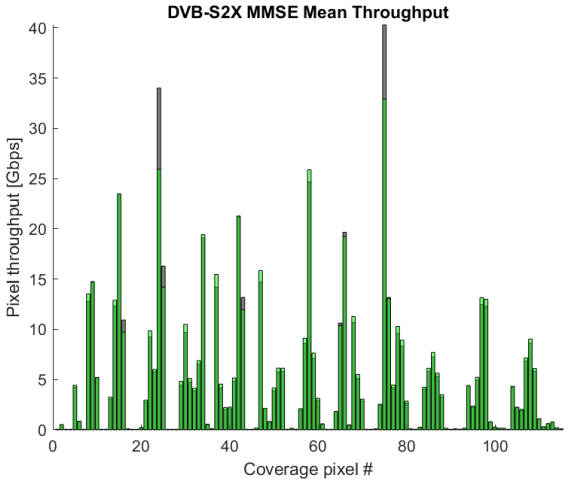

(a) MMSE throughput per pixel for $N_T/N_U = 25$.

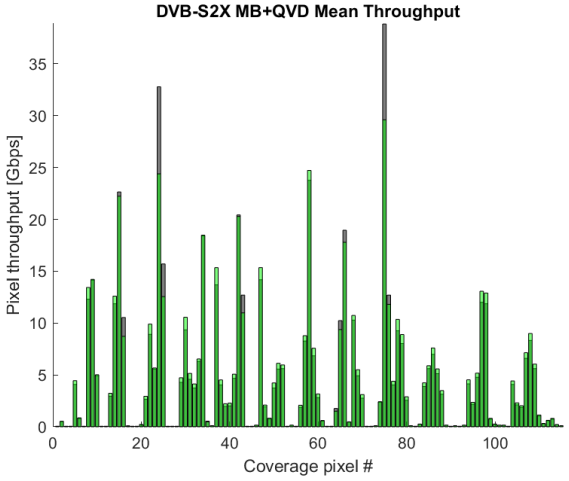

(b) MB+QVD throughput per pixel for $N_T/N_U = 25$.

FIGURE 14. Simulated throughput versus traffic request per coverage pixels, $N_t/N_u = 25$ corresponding to the highest useful traffic condition.

for very large values of $[N_T/N_U]$ the traffic load reduction provides RRM enough "space" to allocate the resources following the requested spatial traffic distribution, although delivering a lower overall system throughput.

Taking into account the previous observations and considering the specific traffic request distribution, the optimum operating point for MB+QVD and MMSE corresponds to $[N_T/N_U]_{opt}$=30 and $[N_T/N_U]_{opt}$=35 respectively. According to the results of Fig. 10 and 11, for these N_T/N_U values a traffic satisfaction factor of 97.3% and 98.6% is achieved for MB+QVD and MMSE respectively.

Figure 12 reports the MB+QVD throughput performance gap versus fully ideal MMSE precoding. By selecting the N_T/N_U value to cross the vertical dash-dotted line corresponding to the target net throughput, the MB+QVD net throughput loss compared to MMSE can be as low as 4.8%. As mentioned before, both M-MIMO techniques can achieve the required throughput with a very good satisfaction factor. Clearly, the net throughput performance gap is higher and around 7.5% for the operating point providing the maximum MB+QVD net throughput. It is also remarked that the MB+QVD gap vs MMSE is lower (3.6%) for the maximum raw throughput. In fact, in this case MB+QVD, although being less capable than MMSE to cover the peak of traffic requests, is still able to generate extra traffic in less interfered pixels. It is interesting to remark that when $N_T/N_U < 15$ (a sub-optimum operating region) the MMSE performance is getting worse than the MB+QVD one.

Figure 13 histograms are presenting, for each sequentially numbered area pixel, the offered system throughput $T_O(l)$ versus the traffic request $T_R(l)$ for the case for which the target useful throughput is achieved corresponding to the previously derived $[N_T/N_U]_{opt}$ values. The dark green bar indicates the useful throughput provided. The light green bar shows the excess throughput provided in a specific area pixel. When present, the gray bar displays the amount of unsatisfied traffic

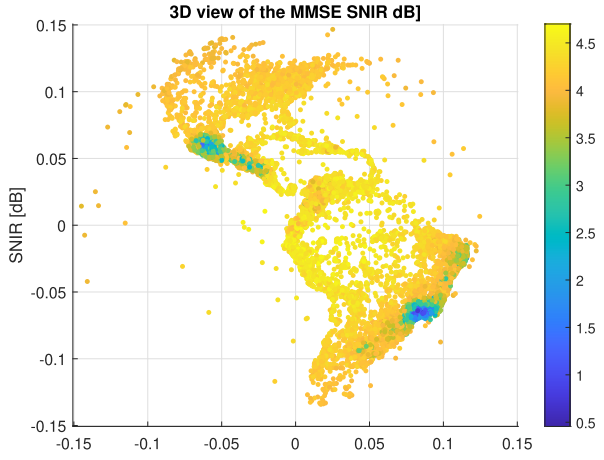

(a) MMSE SNIR for $N_t/N_u = 25$.

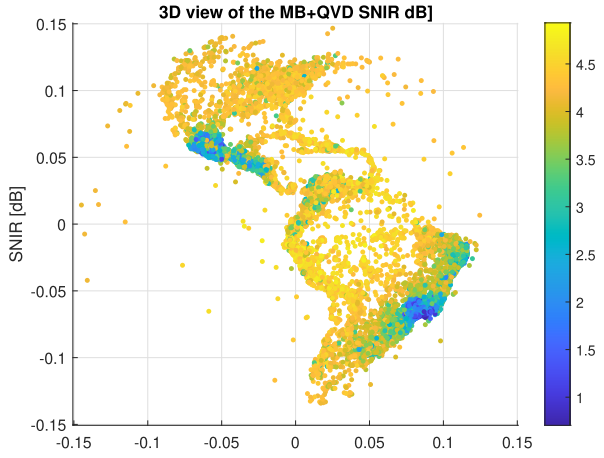

(b) MB+QVD SNIR for $N_t/N_u = 25$.

FIGURE 15. Simulated SNIR over the coverage region corresponding to the highest useful traffic condition.

request. The MMSE and MB+QVD histograms obtained for the respective $[N_T/N_U]_{opt} = [35,\ 30]$ values, confirm the overall good level of traffic request satisfaction achieved. As expected the MMSE shows superior performance for the highest traffic demand coverage area pixels where the Fig. 13 histograms show some visible gap for the offered throughput.

Figure 14 histograms show the situation when the useful throughput is maximum for MMSE and MB+QVD i.e. when $[N_T/N_U]_{max} = 25$. As we can see in this case, where the total traffic requested is larger, the RRM is not able to satisfy the traffic request in high traffic density pixels. We observe that MMSE total useful throughput is larger compared to MB+QVD although not being able to fully match the traffic request.

The 3D plots reported in Fig. 15 show the simulated SNIR spatial distribution for MMSE and MB+QVD when the useful throughput is maximum. As expected, the number of pixels showing a lower SNIR are larger in the MB+QVD

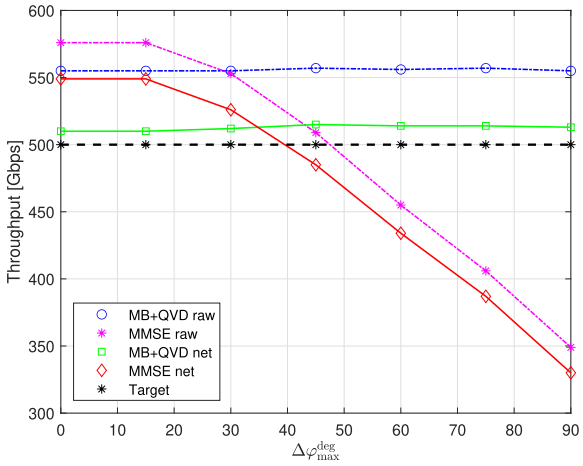

FIGURE 16. Simulated throughput (raw and net) versus the phase calibration error parameter $\Delta\varphi_{max}^{deg}$ assuming $N_T/N_U = 25$, $\Delta A_{max}^{dB} = 2$ dB except when $\Delta\varphi_{max}^{deg} = 0$ to which corresponds $\Delta A_{max}^{dB} = 0$ dB.

case which is not benefiting from the MMSE co-channel interference mitigation capability. It is noted that to match the traffic request, the H-RRM is implementing an irregular frequency reuse scheme, thus leading to a SNIR distribution that is inversely proportional to the traffic request (i.e. higher frequency reuse for the areas with more traffic density).

Finally, in Fig. 16 we report the throughput impact of the matrix $\mathbf{H}$ phase estimation errors in the throughput according to the model described in Sec. III-C. We assume as variable parameter the maximum phase error $\Delta\varphi_{max}^{deg}$ and a fixed amplitude estimation error $\Delta A_{max}^{dB} = 2$ dB. The performance of MB+QVD is independent[7] from $\Delta\varphi_{max}^{deg}$ as this technique is exploiting a fixed grid of beams without any channel matrix estimation. It is clear that up to $\Delta\varphi_{max}^{deg} = 15$ degrees the MMSE performance is almost unchanged. Beyond this value the MMSE throughput declines and when $\Delta\varphi_{max}^{deg} = 40$ degrees the theoretical MMSE advantage versus MB+QVD fully vanishes.

V. CONCLUSION

In this paper we have been extending previous work on the performance analysis of (pragmatic) M-MIMO applicability to broadband satellite access networks. In particular, we have been extending the formulation of the heuristic RRM algorithm to the case of a frequency division colouring approach. We derived the optimal formulation for the MMSE MIMO precoding Lagrange multiplier for both the time and frequency colouring scheme accounting for the current system load.

To derive more realistic performance results we have been enhancing the system model by devising a way to generate an arbitrary traffic distribution based on its two-dimensional spatial probability density function. To enhance the H-RRM algorithm performance, we extended the satellite

[7]The slight MB+QVD throughput performance fluctuation is due to the different Monte Carlo simulation runs.

antenna model for H-RRM by including an accurate sidelobes modelling. We have been assessing the impact of MMSE precoding channel random estimation errors on the system throughput. Finally, we enhanced the system throughput performance analysis to allow spatial traffic request satisfaction analysis.

We developed a novel methodology to derive the optimum operating point of the system for a realistic traffic distribution. It has been shown that the MB+QVD M-MIMO techniques can provide very high level of traffic request satisfaction with marginal loss compared to much more complex ideal MMSE solution.

APPENDIX

A. H-RRM ALGORITHM EXTENSION TO THE GENERIC MULTIPLEXING SCHEME CASE

1) GENERALIZED SYSTEM MODEL

In the following we develop a more general formulation of RRM and beamforming/precoding problem for Multi-User (M-)MIMO forward link communication systems starting from the link and capacity equations. The following sections provide an extension of the algorithm described for the TDM beam hopped case in [17]. The satellite is assumed to transmit to the j-th user by mean of the l-th radio resource (e.g., time frames (slots) in TDM, carriers' frequency in FDM, polarizations, direct-sequence spread-spectrum codes in case of Code Division Multiplexing (CDM) or any combination of these including polarization reuse which allows to double the TDM/FDM/CDM colours). We are interested in determining the link budget for the i-th user when receiving with the k-th radio resource.[8] For this purpose we introduce the generalized power transfer coefficients $s(i,k|j,l)$ (with $i,j=1\ldots N$; $k,l=1\ldots C$) representing the power (normalized to its noise power) received by user i in colour k when the satellite transmits to user j in colour l. We now define the total number of active users (carriers) N as[9]

$$N=\sum_{c=1}^{C} N_U(c). \tag{30}$$

A lexicographic ordering of the indexes (i,k) and (j,l) allows to collect the power transfer coefficients in a generalized power transfer matrix $\tilde{\mathbf{S}}$. It should be noted that this formulation is over-redundant for analysis purposes as a single colour will be associated to each user, i.e. $k=COL(i)$ and $l=COL(j)$. In this case, the generalized (noted with apex G) signal-to-noise, interference-to-noise, and signal-to-noise plus interference ratios become, respectively

$$SNR^G(i)=s\left(i,COL(i)|i,COL(i)\right), \tag{31}$$

$$INR^G(i)=\sum_{j=1,\,j\neq i}^{N} s\left(i,COL(i)|j,COL(j)\right), \tag{32}$$

$$SNIR^G(i)=\frac{s\left(i,COL(i)|j,COL(j)\right)}{1+\sum_{j=1,\,j\neq i}^{N} s\left(i,COL(i)|j,COL(j)\right)}=\frac{SNR^G(i)}{1+INR^G(i)}. \tag{33}$$

The assignment of the colour to the user is the central problem of RRM. To tackle the assignment issue we can imagine that the generalized power transfer coefficient $s(i,k|j,l)$ assumes the meaning of what would be the power received by user i in colour k if the satellite would transmit in colour l for user j.

A user colouring matrix $\mathbf{C}$ of of size $(N\times C)$ can be introduced, with binary entries

$$\mathbf{C}=\begin{bmatrix} c(1,1) & \cdots & c(1,C)\\ \vdots & & \vdots\\ c(N,1) & \cdots & c(N,C)\end{bmatrix}, \tag{34}$$

where

$$c(i,k)=\begin{cases}1 \text{ if } COL(i)=k\\ 0 \quad \text{otherwise}\end{cases}. \tag{35}$$

Also in this case the matrix $\mathbf{C}$ can be seen as a mapping matrix associating users to the respective colours. Considering that the i-th user can be assigned only to one colour, the rows of $\mathbf{C}$ must satisfy the following linear constraint corresponding to one user per colour

$$\sum_{k=1}^{C} c(i,k)=1,\quad i=1,\ldots,N. \tag{36}$$

Making use of the binary entries of the colouring matrix, (31), (32), (33) can be rewritten as, respectively

$$SNR^G(i)=\sum_{k=1}^{C}\sum_{l=1}^{C} c(i,k)s(i,k|i,l)c(i,l), \tag{37}$$

$$INR^G(i)=\sum_{j=1,\,j\neq i}^{N}\sum_{k=1}^{C}\sum_{l=1}^{C} c(i,k)s(i,k|j,l)c(j,l), \tag{38}$$

$$SNIR^G(i)=\frac{\sum_{k=1}^{C}\sum_{l=1}^{C} c(i,k)s(i,k|i,l)c(i,l)}{1+\sum_{j=1,\,j\neq i}^{N}\sum_{k=1}^{C}\sum_{l=1}^{C} c(i,k)s(i,k|j,l)c(j,l)}=\frac{SNR^G(i)}{1+INR^G(i)}. \tag{39}$$

When the generalized power transfer coefficients $s(i,k|j,l)$ are known, the resource management problem can be cast in an Integer Programming problem of the form

$$\underset{c(i,k)}{\text{maximize}}\left\{\sum_{i=1}^{N}\log_2\left[1+\frac{\sum_{k=1}^{C}\sum_{l=1}^{C} c(i,k)s(i,k|i,l)c(i,l)}{1+\sum_{j=1,\,j\neq i}^{N}\sum_{k=1}^{C}\sum_{l=1}^{C} c(i,k)s(i,k|j,l)c(j,l)}\right]\right\}, \tag{40}$$

[8] In the following we will use the term "colour" as a synonym of radio resource.

[9] We prefer to use N instead of N_U to simplify the notation.

$$\text{subject to} \quad \sum_{k=1}^{C} c(i,k) = 1, \quad i = 1, \ldots, N, \\ c(i,k) \in \{0,1\}, \quad i = 1, \ldots, N, \quad k = 1, \ldots, C. \tag{41}$$

While general, this formulation hides the fact that the generalized power transfer coefficients $s(i,k|j,l)$ would depend on the beamforming/precoding vectors selected for each of the j-th user, $\mathbf{w}_j$, and subject to physical feasibility constraints (as total power, and per element power constraints). Indicating with $\mathbf{h}_i^{k|l}$ (with $l, \quad k = 1 \ldots C, \quad i = 1 \ldots N$) the $(N_T \times 1)$ channel row vector representing the complex transfer function between the N_T radiating elements of the satellite antenna array and the user i when the satellite transmits using colour l and the user receives at colour k, we can evaluate the generalized power transfer coefficients as

$$s(i,k|j,l) = \left| \mathbf{h}_i^{k|l} \mathbf{w}_j \right|^2. \tag{42}$$

The most general RRM and precoding/beamforming optimization could then be expressed as the following Mixed Integer Programming problem

$$\underset{c(i,k),\ \mathbf{w}_j}{\text{maximize}} \left\{ \sum_{i=1}^{N} \log_2 \left[1 + \frac{\sum_{k=1}^{C} \sum_{l=1}^{C} c(i,k) \left| \mathbf{h}_i^{l|l} \mathbf{w}_i \right|^2 c(i,l)}{1 + \sum_{j=1, j\neq i}^{N} \sum_{k=1}^{C} \sum_{l=1}^{C} c(i,k) \left| \mathbf{h}_i^{k|l} \mathbf{w}_j \right|^2 c(j,l)} \right] \right\}, \tag{43}$$

$$\text{subject to} \quad \sum_{k=1}^{C} c(i,k) = 1, \quad i = 1, \ldots, N, \\ c(i,k) \in \{0,1\}, \quad i = 1, \ldots, N, \quad k = 1, \ldots, C. \\ \mathbf{w}_j \ \text{ under element/total power constraints} \tag{44}$$

The colour assignment and the beamforming/precoding optimization are coupled problems as the optimal precoding/beamforming depends strongly on the active users sharing the same colour. Additionally, for a certain assignment of users to colours, the optimal precoding/beamforming will be colour dependent (e.g. due to frequency dispersion of the channel row vectors).

The joint optimization of the radio resources and of the precoding/beamforming is thus a problem of formidable complexity which can be practically attacked only adopting pragmatic solutions. It can be observed that the complexity of the problem is reduced if the beamforming weights are known or the problem of their determination can be decoupled from the RRM aspect. In this respect, we could exploit the simplifying hypothesis that each precoding/beamforming vector depends only on the geometry and link conditions of each associated user (they are determined, for user j, at colour l by the channel row vector $\mathbf{h}_j^{l|l}$). We will indicate with $\mathbf{w}(\mathbf{h})$ the mapping function that determines a zero-order approximation of the optimal precoding/beamforming vector given the channel row vector $\mathbf{h}$. Relaxing the per-element/total power constraints, and considering the possible colour dependency of the channel row vector, $\mathbf{h}_i^{k|l}$, we can obtain a formulation of the radio resource optimization which is decoupled from the precoding/beamforming optimization problem. With the substitution

$$s(i,k|j,l) = \left| \mathbf{h}_i^{k|l} \mathbf{w} \left(\mathbf{h}_j^{l|l} \right) \right|^2, \tag{45}$$

and under the precoding/beamforming constraints relaxation, the Mixed Integer Programming problem of (43) collapses into the Integer Programming problem of (40). Once a user colouring matrix $\mathbf{C}$ is found as solution to the Integer Programming problem of (40), the precoding/beamforming optimization and normalization can be performed according to either known techniques (e.g. Matched-Filter, Zero-Forcing, Minimum-Mean-Square-Error, Pragmatic Multi-Beam, etc.) or newly disclosed techniques (i.e. Virtual Distancing and Quantized Virtual Distancing) [17], [18]. Solving the Integer Programming problem of (40) is thus pivotal to find a solution to the general RRM problem. In this respect we can leverage on the results obtained by the authors substituting the Integer Programming problem of the maximization of sum-capacity with the Mixed Integer Quadratic Problem (MIQP) of the minimization of the sum-interference. Also in the general case, the aggregated co-channel interference, evaluated as the total interference-to-noise ratio INR_T^G, can be assumed as a figure of merit of the overall performance and it satisfies the following definition

$$INR_T^G = \sum_{i=1}^{N} INR(i) \\ = \sum_{i=1}^{N} \sum_{j=1,\ j\neq i}^{N} \sum_{k=1}^{C} \sum_{l=1}^{C} c(i,k)\, s(i,k|j,l)\, c(j,l). \tag{46}$$

From the generalized power transfer coefficients $s(i,k|j,l)$ we can obtain the generalized interference coefficients $q(i,k|j,l)$

$$q(i,k|j,l) = \begin{cases} 0 & \text{if } i = j \ \forall\, k,l \\ s(i,k|j,l) & \text{if } i \neq j \ \ \forall\, k,l \end{cases}. \tag{47}$$

Similarly to how the generalized power transfer matrix $\widetilde{\mathbf{S}}$ is organized, we can obtain a generalized interference matrix $\widetilde{\mathbf{Q}}$ of size $[(NC) \times (NC)]$. The matrix $\widetilde{\mathbf{Q}}$ is obtained from the coefficients $q(i,k|j,l)$ with the lexicographic ordering of the indexes (i,k) and (j,l). It is worth noting that in this case, not only the diagonal entries of the matrix $\widetilde{\mathbf{Q}}$ are null, but also all the diagonals of the $(N \times N)$ square submatrices composing $\widetilde{\mathbf{Q}}$.

Vectorizing the matrix $\mathbf{C}$ of size $(N \times C)$ into a column vector vec($\mathbf{C}$) of size $(NC \times 1)$, which is obtained by stacking the columns of $\mathbf{C}$ on top of each other as

$$\text{vec}(\mathbf{C}) \\ = [c(1,1), \ldots, c(N,1), \ldots, c(1,C), \ldots, c(N,C)]^T, \tag{48}$$

the aggregated co-channel interference can be formulated as a quadratic form on the column vector vec(**C**)

$$INR_T^G = \sum_{i=1}^{N}\sum_{j=1}^{N}\sum_{k=1}^{C}\sum_{l=1}^{C} c(i,k)\; q\,(i,k|j,l)\;\; c(j,l)$$
$$= [\text{vec}\,(\mathbf{C})]^T\;\widetilde{\mathbf{Q}}\;\text{vec}\,(\mathbf{C})\,. \tag{49}$$

The approximated resource management problem can be thus cast in a Mixed Integer Quadratic Programming (MIQP) problem of the form

$$\underset{c(i,k)}{\text{minimize}}\left\{[\text{vec}\,(\mathbf{C})]^T\;\;\widetilde{\mathbf{Q}}\;\text{vec}\,(\mathbf{C})\right\}, \tag{50}$$

$$\text{subject to}\quad \sum_{k=1}^{C} c\,(i,k) = 1,\;\; i = 1,\ldots,N$$
$$c\,(i,k) \in \{0,1\}\,,\;\; i = 1,\ldots,N;\;\;\; k = 1,\ldots,C. \tag{51}$$

Before entering in the details of the heuristic optimization of such problem, it is worth discussing some particular form that the generalized interference matrix $\widetilde{\mathbf{Q}}$ can take depending on the nature of the interference.

2) COLOUR-INDEPENDENT / ORTHOGONAL COLOURS

This case identifies the situation where the use of a colour does not generate interference in the other colours and the power transfer coefficients and the interference coefficients do not depend on the colour (e.g. in single-frequency TDM)

$$s\,(i,k|j,l) = \begin{cases} s\,(i|j) & \text{if}\;\; k = l\;\forall\; i,j \\ 0 & \text{if}\;\; k \neq l\;\;\forall\; i,j. \end{cases} \tag{52}$$

In this case the generalized interference matrix $\widetilde{\mathbf{Q}}$ can be written as a block diagonal matrix

$$\widetilde{\mathbf{Q}} = \mathbf{I}\otimes\mathbf{Q} = \begin{bmatrix} \mathbf{Q} & \mathbf{0} & \cdots & \mathbf{0} \\ \mathbf{0} & \ddots & & \\ \vdots & & \mathbf{Q} & \vdots \\ & & \ddots & \mathbf{0} \\ \mathbf{0} & & \mathbf{0} & \mathbf{Q} \end{bmatrix}, \tag{53}$$

which corresponds to the basic case already treated in [17], with

$$\mathbf{Q} = \mathbf{S} - \text{diag}\,\{\text{diag}\,(\mathbf{S})\}\,,\;\; \mathbf{S} = |\mathbf{HW}|^2\,, \tag{54}$$

where $\mathbf{H}$ is the colour independent channel matrix and $\mathbf{W}$ is the precoding/beamforming matrix

$$\mathbf{H} = \begin{bmatrix} \mathbf{h}_1 \\ \vdots \\ \mathbf{h}_N \end{bmatrix}, \tag{55}$$

$$\mathbf{W} = [\mathbf{w}_1\;\;\ldots\;\;\mathbf{w}_N]\,, \tag{56}$$

and the squared absolute value operation $|\;\;|^2$ on the matrix has to be performed entry-wise.

3) COLOUR-DEPENDENT / ORTHOGONAL COLOURS

This case identifies the situation where the use of a colour does not generate interference in the other colours but the power transfer coefficients and the interference coefficients are colour dependent (e.g. in FDM due to the frequency dependency of the payload or antenna, or to the dependency on the polarization but neglecting cross-polarization interference, etc.). In this case we can write

$$s\,(i,k|j,l) = \begin{cases} s^l\,(i|j) & \text{if}\;\; k = l\;\forall\; i,j \\ 0 & \text{if}\;\; k \neq l\;\;\forall\; i,j \end{cases}. \tag{57}$$

Consequently, the generalized interference matrix $\widetilde{\mathbf{Q}}$ can be written as

$$\widetilde{\mathbf{Q}} = \mathbf{I}\otimes\{\mathbf{Q}^l\} = \begin{bmatrix} \mathbf{Q}^1 & \mathbf{0} & \cdots & \mathbf{0} \\ \mathbf{0} & \ddots & & \\ \vdots & & \mathbf{Q}^l & \vdots \\ & & \ddots & \mathbf{0} \\ \mathbf{0} & & \mathbf{0} & \mathbf{Q}^N \end{bmatrix}, \tag{58}$$

where the Fino and Algazi Generalized Kronecker Product notation has been used and

$$\mathbf{Q}^l = \mathbf{S}^l - \text{diag}\left\{\text{diag}\left(\mathbf{S}^l\right)\right\}, \quad \mathbf{S}^l = \left|\mathbf{H}^l\mathbf{W}^l\right|^2, \tag{59}$$

where $\mathbf{H}^l$ is the l-colour channel matrix and $\mathbf{W}^l$ is the precoding/beamforming matrix for colour l

$$\mathbf{H}^l = \begin{bmatrix} \mathbf{h}_1^l \\ \vdots \\ \mathbf{h}_N^l \end{bmatrix}, \quad \mathbf{W}^l = \left[\mathbf{w}_1^l\;\;\ldots\;\;\mathbf{w}_N^l\right]. \tag{60}$$

4) COLOUR-DEPENDENT / NON-ORTHOGONAL COLOURS

This case identifies the most general situation where different colours are non-orthogonal and the power transfer coefficients and the interference coefficients can be colour dependent (e.g. in FDM/CDM cases and when polarization reuse schemes are adopted). In this case the generalized interference matrix has non-zero elements also outside the block-diagonal

$$\widetilde{\mathbf{Q}} = \begin{bmatrix} \mathbf{Q}^{1|1} & \mathbf{Q}^{1|2} & \cdots & \mathbf{Q}^{1|N} \\ \mathbf{Q}^{2|1} & \ddots & & \\ \vdots & & \mathbf{Q}^{k|l} & \vdots \\ & & \ddots & \mathbf{0} \\ \mathbf{Q}^{N|1} & & \cdots & \mathbf{Q}^{N|N} \end{bmatrix}, \tag{61}$$

with

$$\mathbf{Q}^{k|l} = \mathbf{S}^{k|l} - \text{diag}\left\{\text{diag}\left(\mathbf{S}^{k|l}\right)\right\}, \quad \mathbf{S}^{k|l} = \left|\mathbf{H}^{k|l}\mathbf{W}^l\right|^2 \tag{62}$$

where $\mathbf{S}^{k|l}$ is the k-colour channel matrix when the satellite transmits at colour l and $\mathbf{W}^l$ is the precoding/beamforming matrix for colour l defined as

$$\mathbf{H}^{k|l} = \begin{bmatrix} \mathbf{h}_1^{k|l} \\ \vdots \\ \mathbf{h}_N^{k|l} \end{bmatrix}, \quad \mathbf{W}^l = \left[\mathbf{w}_1^l\;\;\ldots\;\;\mathbf{w}_N^l\right]. \tag{63}$$

It is worth noting that although not always negligible, the entries of the matrices $\mathbf{H}^{k|l}$ for $k \neq l$, which contribute to the off-block-diagonal part of $\widetilde{\mathbf{Q}}$, are related to a wanted transmission in colour l that is spilled in colour k and could be often considered as a second-order refinement to the block diagonal matrix related to the colour-dependent / orthogonal-colours case.

5) GENERALIZED H-RRM ALGORITHM

Following the line of thought which led us to the development of an efficient heuristic algorithm, also in this case we can introduce an auxiliary co-channel interference matrix $\mathbf{A}$ of size $(N \times C)$ with elements a_i^k representing the aggregated co-channel interference on user i due to the co-frequency interference of all active users in colour k.

$$\mathbf{A} = \begin{bmatrix} a_1^1 & \cdots & a_1^C \\ \vdots & & \vdots \\ a_N^1 & \cdots & a_N^C \end{bmatrix}. \tag{64}$$

The change of notation from $a(i,k)$ to a_i^k will be useful to better understand some of the needed matrix operations. In the basic version of the H-RRM algorithm (which is applicable to the Colour-independent / Orthogonal colours case), the definition of the auxiliary co-channel interference matrix $\mathbf{A}$ is derived from the equation of the aggregated interference

$$INR_T = \mathrm{tr}\left(\mathbf{C}^T \mathbf{Q}\, \mathbf{C}\right), \tag{65}$$

so that the matrix $\mathbf{A}$ takes the form

$$\mathbf{A} = \mathbf{Q}\, \mathbf{C}. \tag{66}$$

Observing that

$$\mathrm{tr}\left(\mathbf{C}^T \mathbf{A}\right) = [\mathrm{vec}\,(\mathbf{C})]^T\, \mathrm{vec}\,(\mathbf{A}), \tag{67}$$

and considering the definition of the auxiliary co-channel interference matrix we get $\mathbf{A}$

$$\mathrm{vec}\,(\mathbf{A}) = \widetilde{\mathbf{Q}}\, \mathrm{vec}\,(\mathbf{C}), \tag{68}$$

we can interpret the aggregated interference equation for the generalized case as

$$INR_T^G = [\mathrm{vec}\,(\mathbf{C})]^T\ \widetilde{\mathbf{Q}}\, \mathrm{vec}\,(\mathbf{C}). \tag{69}$$

The information contained in $\mathbf{A}$ or $\mathrm{vec}\,(\mathbf{A})$ is the same but for homogeneity of description of the heuristic algorithm we can introduce the inverse vectorization operation, $\mathrm{vec}^{-1}(\,)$, which is a re-shaping operation that transforms a vector in a matrix. In the following the argument vectors will be of size $(NC \times 1)$ and the resultant matrix of size $(N \times C)$, such that $\mathrm{vec}^{-1}[\mathrm{vec}\,(\mathbf{A})] = \mathbf{A}$, and

$$\mathbf{A} = \mathrm{vec}^{-1}\left[\widetilde{\mathbf{Q}}\, \mathrm{vec}\,(\mathbf{C})\right]. \tag{70}$$

According to what has been shown for the Colour-independent / Orthogonal-colours case, we can make the assumption that at the n-th iteration a number of users has been assigned to a colour such that the temporary colouring matrix $\mathbf{C}^{(n)}$ satisfies

$$\sum_{k=1}^{C} c^{(n)}(j,k) = \begin{cases} 1 & \text{if user } j \text{ has a colour assigned} \\ 0 & \text{otherwise} \end{cases}. \tag{71}$$

At each iteration we can evaluate the temporary auxiliary matrix $\mathbf{A}^{(n)}$ and select, among the non-assigned users, the one (row) with worst interference and for it the least interfering colour (within the row). The matrix $\mathbf{A}^{(n)}$ is evaluated as

$$\mathbf{A}^{(n)} = \mathrm{vec}^{-1}\left[\widetilde{\mathbf{Q}}\, \mathrm{vec}\left(\mathbf{C}^{(n)}\right)\right]. \tag{72}$$

Together with the different inputs (i.e. collection of matrices $\{\mathbf{Q}^l\}$ or the full generalized interference matrix $\widetilde{\mathbf{Q}}$ instead of the single interference matrix $\mathbf{Q}$), the above generalization for the evaluation of the temporary auxiliary matrix $\mathbf{A}^{(n)}$ are the only modifications that need to be applied to the heuristic colouring algorithm.

The development of a fast version of the algorithm is based on the expansion

$$\mathbf{C}^{(n+1)} = \mathbf{C}^{(n)} + \mathbf{\Delta C}^{(n)}, \tag{73}$$

$$\begin{aligned} \mathbf{A}^{(n+1)} &= \mathrm{vec}^{-1}\left[\widetilde{\mathbf{Q}}\, \mathrm{vec}\left(\mathbf{C}^{(n)} + \mathbf{\Delta C}^{(n)}\right)\right] \\ &= \mathrm{vec}^{-1}\left[\widetilde{\mathbf{Q}}\, \mathrm{vec}\left(\mathbf{C}^{(n)}\right)\right] \\ &\quad + \mathrm{vec}^{-1}\left[\widetilde{\mathbf{Q}}\, \mathrm{vec}\left(\mathbf{\Delta C}^{(n)}\right)\right] \\ &= \mathbf{A}^{(n)} + \mathbf{\Delta A}^{(n)}. \end{aligned} \tag{74}$$

To understand the form of $\mathbf{\Delta A}^{(n)}$ we can observe that rewriting the user colouring matrix $\mathbf{C}$ as column vectors $\mathbf{c}_l^C$

$$\mathbf{C} = \left[\mathbf{c}_1^C \ \cdots\ \mathbf{c}_l^C \ \cdots\ \mathbf{c}_C^C\right], \tag{75}$$

the vectorization $\mathrm{vec}\,(\mathbf{C})$ takes the form

$$\mathrm{vec}\,(\mathbf{C}) = \begin{bmatrix} \mathbf{c}_1^C \\ \vdots \\ \mathbf{c}_l^C \\ \vdots \\ \mathbf{c}_C^C \end{bmatrix}, \tag{76}$$

and the matrix-vector product, $\widetilde{\mathbf{Q}}\, \mathrm{vec}\,(\mathbf{C})$, becomes

$$\widetilde{\mathbf{Q}}\mathrm{vec}\,(\mathbf{C}) = \begin{bmatrix} \mathbf{Q}^{1|1} & \mathbf{Q}^{1|2} & & \cdots & \mathbf{Q}^{1|N} \\ \mathbf{Q}^{2|1} & \ddots & & & \\ \vdots & & \mathbf{Q}^{k|l} & & \vdots \\ & & & \ddots & \mathbf{0} \\ \mathbf{Q}^{N|1} & & & \cdots & \mathbf{Q}^{N|N} \end{bmatrix} \begin{bmatrix} \mathbf{c}_1^C \\ \vdots \\ \mathbf{c}_l^C \\ \vdots \\ \mathbf{c}_C^C \end{bmatrix}$$

$$= \begin{bmatrix} \sum_{l=1}^{C} \mathbf{Q}^{1|l}\mathbf{c}_l^C \\ \vdots \\ \sum_{l=1}^{C} \mathbf{Q}^{k|l}\mathbf{c}_l^C \\ \vdots \\ \sum_{l=1}^{C} \mathbf{Q}^{C|l}\mathbf{c}_l^C \end{bmatrix}. \tag{77}$$

Finally

$$\begin{aligned} &\mathrm{vec}^{-1}\left[\widetilde{\mathbf{Q}}\,\mathrm{vec}\left(\mathbf{C}^{(n)}\right)\right] \\ &= \left[\sum_{l=1}^{C}\mathbf{Q}^{1|l}\mathbf{c}_l^C \cdots \sum_{l=1}^{C}\mathbf{Q}^{k|l}\mathbf{c}_l^C \cdots \sum_{l=1}^{C}\mathbf{Q}^{C|l}\mathbf{c}_l^C\right]. \end{aligned} \tag{78}$$

At iteration (n) colour $l^{(n)}$ is assigned to user $j^{(n)}$. The only unit entry element of $\Delta\mathbf{C}^{(n)}$ is in the one with index $(j^{(n)},l^{(n)})$, and

$$\Delta\mathbf{C}^{(n)} = \left[\mathbf{0} \cdots \Delta\mathbf{c}^C_{l^{(n)}} \cdots \mathbf{0}\right], \tag{79}$$

substituting

$$\begin{aligned} \Delta\mathbf{A}^{(n)} &= \mathrm{vec}^{-1}\left[\widetilde{\mathbf{Q}}\,\mathrm{vec}\left(\Delta\mathbf{C}^{(n)}\right)\right] \\ &= \left[\mathbf{Q}^{1|l^{(n)}}\Delta\boldsymbol{c}^C_{l^{(n)}} \cdots \mathbf{Q}^{k|l^{(n)}}\Delta\boldsymbol{c}^C_{l^{(n)}} \cdots \mathbf{Q}^{C|l^{(n)}}\Delta\boldsymbol{c}^C_{l^{(n)}}\right] \\ &= \left[\left[\mathbf{Q}^{1|l^{(n)}}\right]^C_{j^{(n)}} \cdots \left[\mathbf{Q}^{k|l^{(n)}}\right]^C_{j^{(n)}} \cdots \left[\mathbf{Q}^{C|l^{(n)}}\right]^C_{j^{(n)}}\right]. \end{aligned} \tag{80}$$

The notation $[\mathbf{Q}]^C_j$ indicates the j-th column of the matrix $\mathbf{Q}$. Equation (80) can be interpreted as the fact that the assignment of colour $l^{(n)}$ to user $j^{(n)}$ increases each colour column vector interference of with relevant contribution. This equation provides also a fast update of the auxiliary matrix $\mathbf{A}^{(n)}$ which avoids any matrix multiplication with substantial computational speed-up. Depending on the case applicable to the generalized interference matrix $\widetilde{\mathbf{Q}}$, further simplification can be performed.

6) COLOUR-INDEPENDENT/ORTHOGONAL COLOURS

In this case, according to (52)

$$\mathbf{Q}^{k|l} = \begin{cases} \mathbf{Q} & \text{for } k = l \ \ \forall\, k, l \\ \mathbf{0} & \text{otherwise} \end{cases}. \tag{81}$$

The update of the auxiliary matrix $\mathbf{A}^{(n)}$ becomes

$$\Delta\mathbf{A}^{(n)} = \begin{bmatrix} \mathbf{0} & \cdots & \underset{\downarrow}{l^{(n)}} & \cdots & \mathbf{0} \\ & & [\mathbf{Q}]^C_{j^{(n)}} & & \end{bmatrix}. \tag{82}$$

which corresponds to the basic case already treated.

7) COLOUR-DEPENDENT / ORTHOGONAL COLOURS

In this case, according to (57)

$$\mathbf{Q}^{k|l} = \begin{cases} \mathbf{Q}^l & \text{for } k = l \\ \mathbf{0} & \text{otherwise.} \end{cases} \tag{83}$$

The update of the auxiliary matrix $\mathbf{A}^{(n)}$ becomes

$$\Delta\mathbf{A}^{(n)} = \begin{bmatrix} \mathbf{0} & \cdots & \underset{\downarrow}{l^{(n)}} & \cdots & \mathbf{0} \\ & & \left[\mathbf{Q}^{l^{(n)}}\right]^C_{j^{(n)}} & & \end{bmatrix}. \tag{84}$$

8) COLOUR-DEPENDENT/NON-ORTHOGONAL COLOURS

In this case the generalized interference matrix $\widetilde{\mathbf{Q}}$ is broadly non null and composed of block sub-matrices $\mathbf{Q}^{k|l}$, thus the following equation applies

$$\Delta\mathbf{A}^{(n)} = \begin{bmatrix} \underset{\downarrow}{1} & \cdots & \underset{\downarrow}{k} & \cdots & \underset{\downarrow}{C} \\ \left[\mathbf{Q}^{1|l^{(n)}}\right]^C_{j^{(n)}} & \cdots & \left[\mathbf{Q}^{k|l^{(n)}}\right]^C_{j^{(n)}} & \cdots & \left[\mathbf{Q}^{C|l^{(n)}}\right]^C_{j^{(n)}} \end{bmatrix}. \tag{85}$$

REFERENCES

[1] L. Cottatellucci, M. Debbah, G. Gallinaro, R. Mueller, M. Neri, and R. Rinaldo, "Interference mitigation techniques for broadband satellite systems," in *Proc. 24th AIAA Int. Commun. Satell. Syst. Conf.*, Jun. 2006, pp. 1–13.

[2] G. Taricco, "Linear precoding methods for multi-beam broadband satellite systems," in *Proc. 20th Eur. Wireless Conf.*, May 2014, pp. 1–6.

[3] P. Arapoglou, A. Ginesi, S. Cioni, S. Erl, F. Clazzer, S. Andrenacci, and A. Vanelli-Coralli, "DVB-S2X-enabled precoding for high throughput satellite systems," *Int. J. Satell. Commun. Netw.*, vol. 34, no. 3, pp. 439–455, May 2016.

[4] D. Christopoulos, S. Chatzinotas, G. Zheng, J. Grotz, and B. Ottersten, "Linear and nonlinear techniques for multibeam joint processing in satellite communications," *EURASIP J. Wireless Commun. Netw.*, vol. 162, no. 1, pp. 1–13, May 2012.

[5] V. Joroughi, M. Á. Vázquez, and A. I. Pérez-Neira, "Precoding in multigateway multibeam satellite systems," *IEEE Trans. Wireless Commun.*, vol. 15, no. 7, pp. 4944–4956, Jul. 2016.

[6] A. Ginesi, E. Re, and P. D. Arapoglou, "Joint beam hopping and precoding in HTS systems," in *Wireless and Satellite Systems* (Lecture Notes of the Institute for Computer Sciences, Social Informatics and Telecommunications Engineering), vol. 231, P. Pillai, K. Sithamparanathan, G. Giambene, M. Vazquez, P. Mitchell, Eds. Cham, Switzerland: Springer, 2017, pp. 43–51.

[7] G. Cocco, T. de Cola, M. Angelone, Z. Katona, and S. Erl, "Radio resource management optimization of flexible satellite payloads for DVB-S2 systems," *IEEE Trans. Broadcast.*, vol. 64, no. 2, pp. 266–280, Jun. 2018.

[8] C. N. Efrem and A. D. Panagopoulos, "Dynamic energy-efficient power allocation in multibeam satellite systems," *IEEE Wireless Commun. Lett.*, vol. 9, no. 2, pp. 228–231, Feb. 2020.

[9] M. G. Kibria, E. Lagunas, N. Maturo, D. Spano, and S. Chatzinotas, "Precoded cluster hopping in multi-beam high throughput satellite systems," in *Proc. IEEE Global Commun. Conf. (GLOBECOM)*, Dec. 2019, pp. 1–6.

[10] L. Chen, V. N. Ha, E. Lagunas, L. Wu, S. Chatzinotas, and B. Ottersten, "The next generation of beam hopping satellite systems: Dynamic beam illumination with selective precoding," *IEEE Trans. Wireless Commun.*, vol. 22, no. 4, pp. 2666–2682, Apr. 2023.

[11] A. I. Aravanis, M. R. B. Shankar, P.-D. Arapoglou, G. Danoy, P. G. Cottis, and B. Ottersten, "Power allocation in multibeam satellite systems: A two-stage multi-objective optimization," *IEEE Trans. Wireless Commun.*, vol. 14, no. 6, pp. 3171–3182, Jun. 2015.

[12] P. Angeletti and R. De Gaudenzi, "A pragmatic approach to massive MIMO for broadband communication satellites," *IEEE Access*, vol. 8, pp. 132212–132236, Jul. 2020.

[13] L. You, K.-X. Li, J. Wang, X. Gao, X.-G. Xia, and B. Ottersten, "Massive MIMO transmission for LEO satellite communications," *IEEE J. Sel. Areas Commun.*, vol. 38, no. 8, pp. 1851–1865, Aug. 2020.

[14] L. You, X. Qiang, K.-X. Li, C. G. Tsinos, W. Wang, X. Gao, and B. Ottersten, "Hybrid analog/digital precoding for downlink massive MIMO LEO satellite communications," 2022, *arXiv:2201.06281*.
[15] J. Palacios, N. González-Prelcic, C. Mosquera, T. Shimizu, and C.-H. Wang, "A hybrid beamforming design for massive MIMO LEO satellite communications," *Frontiers Space Technol.*, vol. 2, pp. 1–14, Sep. 2021.
[16] E. Björnson, E. G. Larsson, and T. L. Marzetta, "Massive MIMO: Ten myths and one critical question," *IEEE Commun. Mag.*, vol. 54, no. 2, pp. 114–123, Feb. 2016.
[17] P. Angeletti and R. D. Gaudenzi, "Heuristic radio resource management for massive MIMO in satellite broadband communication networks," *IEEE Access*, vol. 9, pp. 147164–147190, Oct. 2021.
[18] P. Angeletti and R. De Gaudenzi, "Virtual distancing: A beam-steering technique for interference reduction in multibeam antennas," in *Proc. IEEE Int. Symp. Phased Array Syst. Technol. (PAST)*, Oct. 2022, pp. 1–8.
[19] *Digital Video Broadcasting (DVB); Second Generation Framing Structure, Channel Coding and Modulation Systems for Broadcasting, Interactive Services, News Gathering and Other Broadband Satellite Applications; Part 2: DVB-S2 Extensions (DVB-S2X)*, Standard ETSI EN 302 307-2 V1.1.1, Oct. 2010.
[20] C. B. Peel, B. M. Hochwald, and A. L. Swindlehurst, "A vector-perturbation technique for near-capacity multiantenna multiuser communication—Part I: Channel inversion and regularization," *IEEE Trans. Commun.*, vol. 53, no. 1, pp. 195–202, Jan. 2005.
[21] M. Joham, W. Utschick, and J. A. Nossek, "Linear transmit processing in MIMO communications systems," *IEEE Trans. Signal Process.*, vol. 53, no. 8, pp. 2700–2712, Aug. 2005.
[22] P. Viswanath and D. N. C. Tse, "Sum capacity of the vector Gaussian broadcast channel and uplink–downlink duality," *IEEE Trans. Inf. Theory*, vol. 49, no. 8, pp. 1912–1921, Aug. 2003.
[23] L. Devroye, *Non-Uniform Random Variate Generation*. New York, NY, USA: Springer-Verlag, 1986.
[24] R. R. Bate, D. D. Mueller, J. E. White, and W. W. Saylor, *Fundamentals of Astrodynamics*. New York, NY, USA: Dover, 1971.
[25] R. De Gaudenzi, P. Angeletti, D. Petrolati, and E. Re, "Future technologies for very high throughput satellite systems," *Int. J. Satell. Commun. Netw.*, vol. 38, no. 2, pp. 141–161, Mar. 2020.
[26] National Aeronautics and Space Administration, Socioeconomic Data and Applications Center (SEDAC). *Gridded Population World (GPW) V3*.l Accessed: 2015. [Online]. Available: http://sedac.ciesin.columbia.edu/data/set/gpw-v3-population-count-future-estimates/data-download
[27] P. Angeletti, "Multiple beams from planar arrays," *IEEE Trans. Antennas Propag.*, vol. 62, no. 4, pp. 1750–1761, Apr. 2014.
[28] Y. Lo and S. Lee, "Affine transformation and its application to antenna arrays," *IEEE Trans. Antennas Propag.*, vol. AP-13, no. 6, pp. 890–896, Nov. 1965.
[29] D. M. Sazonov, *Microwave Circuits and Antennas*. Odense, Denmark: MIR, 1990.
[30] Y. Rahmat-Samii, P. Cramer, K. Woo, and S. Lee, "Realizable feed-element patterns for multibeam reflector antenna analysis," *IEEE Trans. Antennas Propag.*, vol. AP-29, no. 6, pp. 961–963, Nov. 1981.
[31] P. Angeletti, F. Frezza, R. Vescovo, and G. Toso, "On the directivity of planar arrays wit $\cos^q(\theta)$ element patterns," in *Proc. 30th ESA Antenna Workshop*, ESA/ESTEC Noordwijk, The Netherlands, May 2008, pp. 1–6.
[32] S. D'Addio and P. Angeletti, "A survey of calibration methods for satellite payloads based on active front-ends," in *Proc. ESA Antenna Workshop Antennas Space Appl.*, Noordwijk, The Netherlands, Oct. 2010, pp. 1–4.

PIERO ANGELETTI (Senior Member, IEEE) received the Laurea degree (summa cum laude) in electronics engineering from the University of Ancona, Italy, in 1996, and the Ph.D. degree in electromagnetism from the University of Rome "La Sapienza," Italy, in 2010. He has more than 20 years of experience in RF systems engineering and technical management encompasses conceptual/architectural design, trade-offs, detailed design, production, integration and testing of satellite payloads and active antenna systems for commercial/military telecommunications and navigation (spanning all the operating bands and set of applications) as well as for multifunction RADARs, and electronic counter measure systems. He is currently a Member of the Technical Staff with the European Space Research and Technology Center (ESTEC), European Space Agency, Noordwijk, The Netherlands. He is the Head of the Radio Frequency Payloads and Technology Division, ESA Directorate of Technology, Engineering and Quality (TEC), which is responsible for RF payloads, instruments and relevant technologies. In particular, he oversees ESA research and development activities related to flexible satellite payloads, RF front-ends, and on-board digital processors. He has authored/coauthored over 300 technical reports, book chapters, and papers published in peer-reviewed professional journals and international conferences' proceedings. He holds several patents related to satellite payload and antenna technology. Together with Giovanni Toso, he is a Instructor of the course on "Multibeam Antennas and Beamforming Networks," which has been offered at main IEEE and European microwaves, wireless and antenna conferences (IEEE APS, IEEE IMS, EuMW, EuCAP, IEEE ICWITS, and ESA Internal University), since 2012. In 2022, he received the S. A. Schelkunoff Award by the IEEE Antennas and Propagation Society for the Best IEEE TAP Paper Published, in 2021, Angeletti and Lizarraga, "Traffic Balancing Multibeam Antennas for Communication Satellites."

RICCARDO DE GAUDENZI (Fellow, IEEE) received the master's degree (cum laude) in electronic engineering from the University of Pisa, Italy, in 1985, the Ph.D. degree from the Technical University of Delft, The Netherlands, in 1999, and the Communication Engineering Master degree (Hons.) from the University of Parma, in 2021. From 1986 to 1988, he was with the Stations and Communications Engineering Department, European Space Agency (ESA), Darmstadt, Germany, where he was involved in satellite telemetry, tracking and control (TT&C) ground systems design and testing. In 1988, he joined the ESA's Research and Technology Centre (ESTEC), Noordwijk, The Netherlands, where he has been covering several technical and managerial positions inside the Directorate of Technology, Engineering and Quality. He is currently the Head of the ESA's Electrical Engineering Department. The department covers radio-frequency systems and payloads for navigation, telecommunication TT&C and Earth observation, EEE components and microelectronics, data handling systems, power systems and energy sources, electromagnetic compatibility, and space environments and their effects. He has been responsible for a large number of research and development activities for TT&C, telecom and navigation applications. He has published more than 140 scientific papers and owns more than 30 patents. In 1996, he spent one year with Qualcomm Inc., San Diego, USA, in the Globalstar LEO project system group under an ESA fellowship. His current research interests include efficient digital modulation and multiple access techniques for fixed and mobile satellite services, synchronization topics, adaptive interference mitigation techniques, and communication systems simulation techniques. He actively contributed to the development and the demonstration of the ETSI S-UMTS Family A, S-MIM, DVB-S2, DVB-S2X, DVB-RCS2, and DVB-SH standards. He was a co-recipient of the 2003 and 2008 Jack Neubauer Memorial Award Best Paper from the IEEE Vehicular Technology Society. He has been awarded the American Institute of Aeronautics and Astronautics (AIAA) 2022 Aerospace Communications Award. From 2001 to 2005, he served as an Associate Editor for CDMA and Synchronization for IEEE TRANSACTIONS ON COMMUNICATIONS and the *Journal of Communications and Networks*.